

August 2017

Modeling Gravitational-wave Sources for Pulsar Timing Arrays

Joseph Simon

University of Wisconsin-Milwaukee

Follow this and additional works at: <https://dc.uwm.edu/etd>



Part of the [Astrophysics and Astronomy Commons](#), and the [Physics Commons](#)

Recommended Citation

Simon, Joseph, "Modeling Gravitational-wave Sources for Pulsar Timing Arrays" (2017). *Theses and Dissertations*. 1700.
<https://dc.uwm.edu/etd/1700>

This Dissertation is brought to you for free and open access by UWM Digital Commons. It has been accepted for inclusion in Theses and Dissertations by an authorized administrator of UWM Digital Commons. For more information, please contact open-access@uwm.edu.

MODELING GRAVITATIONAL-WAVE SOURCES FOR
PULSAR TIMING ARRAYS

by

Joseph J. Simon

A DISSERTATION SUBMITTED IN
PARTIAL FULFILLMENT OF THE
REQUIREMENTS FOR THE DEGREE OF

DOCTOR OF PHILOSOPHY
IN PHYSICS

at

The University of Wisconsin–Milwaukee
August 2017

ABSTRACT

MODELING GRAVITATIONAL-WAVE SOURCES FOR PULSAR TIMING ARRAYS

by

Joseph J. Simon

The University of Wisconsin–Milwaukee, 2017
Under the Supervision of Professor Xavier Siemens

The recent direct detections of gravitational waves (GWs) from merging black holes by the Laser Interferometer Gravitational-wave Observatory (LIGO) marks the beginning of the era of GW astronomy and promises to transform fundamental physics. In the coming years, there is hope for detections across the mass scale of binary black holes. Pulsar Timing Arrays (PTAs) are galactic-scale low-frequency (nHz - μ Hz) GW observatories, which aim to directly detect GWs from binary supermassive black holes (SMBHs) ($\gtrsim 10^7 M_\odot$). The frequency and black hole mass range that PTAs are sensitive to is orders of magnitude different from those LIGO is observing, making PTAs a comparable observatory on the GW spectrum. Understanding the link between binary SMBHs and the gravitational radiation detected by PTAs is crucial to the community's capability of making meaningful scientific statements using PTA observations. This dissertation discusses the creation of a state-of-the-art observational-based simulation framework built to provide critical answers to many open questions surrounding the link between PTA data and binary SMBHs.

Binary SMBHs are predicted products of galaxy mergers, and are a crucial step in galaxy formation theories. Recent PTA upper limits on the gravitational radiation in the nanohertz frequency band are impacting our understanding of the binary SMBH population. But as upper limits grow more constraining, what can be implied about galaxy evolution? In this dissertation, I will provide insights into this question by investigating

which astrophysical parameters have the largest impact on GW predictions, developing direct translations between PTA limits and measured values for the parameters of galaxy evolution, and exploring how the use of different galaxy evolution parameters effects the characterization of the GW signal.

During the extended interaction between SMBHs and their host galaxy throughout inspiral, there is the potential for many electromagnetic tracers to accompany the binary's evolution. This dissertation also incorporates models of electromagnetic radiation from binary SMBHs to investigate the potential for jointly detecting a binary's electromagnetic and gravitational radiation. The detection of a single 'multi-messenger' source would provide a unique window into a pivotal stage of galaxy evolution, and would revolutionize the understanding of late-stage galaxy evolution.

TABLE OF CONTENTS

List Of Figures	vii
Acknowledgments	ix
Preface	xi
1 Introduction	1
1.1 The dawn of gravitational-wave astronomy	1
1.2 How do pulsar timing arrays detect gravitational waves?	4
1.3 What are the gravitational wave sources that pulsar timing arrays can detect?	6
1.4 Dissertation Outline	9
2 Building A Model for the Gravitational Wave Background from Binary Supermassive Black Holes	11
2.1 The Gravitational Wave Background	12
2.2 Determining The Merger Rate	14
2.3 Inferring the Black Hole Mass Function	15
2.3.1 GSMF and M_{\bullet} - M_{bulge}	16
2.3.2 VDF and M_{\bullet} - σ	18
2.4 Binary Black Hole Dynamics	18
2.4.1 Stellar Environments	21
2.4.2 Gravitational Radiation	22
2.4.3 Binary Stalling	23
2.5 Gravitational Radiation from Binary SMBH	24
2.6 The PTA Strain Spectrum	25
3 Predictions for the Gravitational Wave Background from Binary Supermassive Black Holes	30
3.1 Predictions for A_{yr} : Fiducial Model	30

3.1.1	\mathcal{R}_{Gal} Constraints	31
3.1.2	Φ_{gsmf} Observations	32
3.1.3	The M_{\bullet} - M_{bulge} Relation	33
3.1.4	A_{yr} Distribution: Fiducial Model	34
3.1.5	Relative effects of GSMF, f_{pair} , and M_{\bullet} - M_{bulge} on A_{yr}	38
3.1.6	Conclusions: Fiducial Model	41
3.2	Predictions for A_{yr} : Φ_{vdf} vs. Φ_{gsmf}	41
3.2.1	Φ_{vdf} Constraints	42
3.2.2	The M_{\bullet} - σ Relation	43
3.2.3	Variations in M_{\bullet} from M_{\bullet} - σ vs. M_{\bullet} - M_{bulge}	43
3.2.4	A_{yr} Distribution: Comparing Φ_{vdf} vs. Φ_{gsmf}	44
3.2.5	Spectral Shape: Comparing Φ_{vdf} vs. Φ_{gsmf}	47
3.3	Spectral Shape from Binary Black Hole Dynamics	50
3.3.1	Stellar Scattering & Eccentricity Evolution	50
3.3.2	Predictions for Full Spectra	52
4	Astrophysical Interpretation of Pulsar Timing Array Limits	54
4.1	Translating GWB Limits and Astrophysical Parameters	54
4.1.1	GW limits and the Black Hole - Host Galaxy Relation	55
4.1.2	GW limits and Stalling Binaries	56
4.2	Limiting M_{\bullet} - M_{bulge} and stalling timescale with PTA constraints	57
4.2.1	Constraining α , β , and ϵ for the M_{\bullet} - M_{bulge} relation with PTAs	58
4.2.2	Reconciling PTA limits with M_{\bullet} - M_{bulge} measurements	59
4.3	Limiting the multidimensional parameter space of binary evolution using Gaussian Process Regression	65
5	Electromagnetic Counterparts for Binary Supermassive Black Holes	67
5.1	Incorporating Models for Dual AGN	67
5.1.1	Dual Radio AGN	68
5.1.2	Peculiar Emission Lines	69
5.2	Predictions for ‘Multi-Messenger’ Sources in the PTA Band	69

6 Summary	73
6.1 Future Work	75
6.1.1 Expanding Models for Black Hole Mass	75
6.1.2 Incorporating Electromagnetic Observations	75
Bibliography	77
Curriculum Vitae	82

LIST OF FIGURES

1	The Gravitational Wave Sky	3
2	Central Black Hole - Host Galaxy Relation	7
3	Timescales Of Binary Dynamics	19
4	Relative Power Radiated at n th Harmonic for Eccentric Binary	25
5	Variation in M_{\bullet} - M_{bulge} correlations in the literature	34
6	A_{yr} Distribution: Fiducial Model	35
7	Fractional contribution to A_{yr} , in fiducial model, as a function of chirp mass, M_c	36
8	Fractional contributions to A_{yr} , in fiducial model, as a function of redshift, z	37
9	Error contribution to A_{yr} , in fiducial model, from observations of galaxy evolution parameters	39
10	Influence of f_{bulge} on A_{yr}	40
11	M_{\bullet} Predictions: Comparison between M_{\bullet} - M_{bulge} and M_{\bullet} - σ	44
12	A_{yr} Distribution: Comparison between Φ_{vdf} and Φ_{gsmf}	45
13	Fractional contribution to A_{yr} , comparison between Φ_{vdf} and Φ_{gsmf} , as a function of chirp mass, M_c	46
14	Strain Spectra Comparison: Φ_{vdf} vs. Φ_{gsmf}	48
15	Strain Spectra Comparison with Turn-over: Φ_{vdf} vs. Φ_{gsmf}	49
16	Model for Eccentricity Evolution Across Parameter Space for ρ and e_0	51
17	Characteristic strain spectra for binary populations under various astrophysical conditions	53
18	Mapping of GWB amplitude to M_{\bullet} - M_{bulge} parameters α and β	55
19	Relative scaling of A_{yr} as a function of the intrinsic scatter, ϵ , of the M_{\bullet} - M_{bulge} relation	56
20	Mapping of GWB amplitude to M_{\bullet} - M_{bulge} parameters α and ϵ	57
21	Effect of SMBH binary stalling time on the expected amplitude of the GWB.	58

22	Translation of marginalized posterior distributions of A_{yr} into the black hole - host galaxy parameter space	60
23	Translations of upper limits on A_{yr} into the parameter space α - ϵ	61
24	Translation of the marginalized posterior distribution of A_{yr} into a probability distribution of T_{stall}	62
25	Joint Constraints on ρ and e_0	66
26	Strain Spectra with Individual Binaries and PTA Limits for Resolvable Sources	70
27	Distributions of Dual Radio AGN	71
28	Distributions of Peculiar Emission Line Sources	72
29	Strain Spectra with Potential Multi-Messenger Sources and PTA Limits for Resolvable Sources	72

ACKNOWLEDGMENTS

Many african proverbs have been loosely translated to, '*it takes a village to raise a child.*' That sentiment was true throughout my upbringing and it has held true through my years in graduate school. I am incredibly grateful to the many villages that have supported me, taught me, and lifted me up, making it possible for me to achieve my goals.

I grew up in the village of the self-proclaimed 'cool, young faculty' at Susquehanna University, a small liberal arts college in rural Pennsylvania, in the 1990s. This group of early career PhDs taught me that not only was the acquisition of knowledge an exciting and worthy pursuit, but more importantly, the community of those who sought to gather and impart knowledge was respectfully welcoming, full of intriguing discussion and lively banter, and a fun place to belong. For me, the leader of this village was my mother whose limitless support and constant encouragement have helped propel me to the completion of this degree. She has instilled in me her mantra, '*always have options*'. Keeping to those words is a main reason why I had the opportunity to complete a doctorate after taking years off to pursue a career in technical theater. My mother's fierce determination to create a safe, comfortable place for me to grow-up while also pursuing her own career goals is a continued inspiration to me as I carve my own career path. There are too many members of the SU community who have had lasting impacts on my life to name them all here, but I would like to highlight a special few whose insights were pivotal to the completion of this degree: Mr. Andy, who has always reminded me to breathe, and that '*remembering is an act of relaxation*'; M.L., who first introduced me to research and the frustrations of an unproven hypothesis; Chris, who let a high school student play with super cool chemistry toys; and the entire D&D crew, who have always allowed this 13 year old boy to storm the keep, time and again.

Through graduate school I have been a part of the village that is the NANOGrav collaboration. I am grateful for the introduction to this group provided to me by Dr. Andrea Lommen, my undergraduate advisor. She took a kindred spirit, who had run away to the circus of professional theater, and launched me down the path to graduate school. The community of post-docs and graduate students in NANOGrav took me under

their wings and continue to encourage me. I am particularly indebted to Dr. Sarah Burke-Spolaor, who sent me an email of partially formed ideas and has let me run wild with a handful of them. At UWM, I am thankful for the entire graduate school community that helped shepherd me through the last five years. Dr. Xavier Siemens, my graduate advisor, gave me the freedom to pursue the research that was most exciting to me, and continues to encourage me to tackle interesting areas of inquiry, even when they are outside of his expertise. CGCA post-docs, especially Chris, Megan, Danielle and Joe, always had their doors open and patiently listened to me ramble on about half formed ideas or seemingly nonsensical computer errors. My officemates, especially Dan, Eric, Lyndsey and Alex, were always up for long and rambling conversations about anything from latest research results to current world affairs. I have been fortunate to be a member of the CGCA family and am grateful for the many friendships I have forged.

Finally, I have been loved and supported throughout all of this by my most personal village: my family. I am blessed to have a myriad of extended family who have all championed me in their own way towards the completion of this degree. I am incredibly fortunate to have found an equal partner in my wife, Anne Jude. She has been the cornerstone for our family holding everything together seamlessly even when homework seemed insurmountable, computer's crashed, codes didn't run, and all of the other apparent crisis of a graduate student came to call. Thank you for persistently reminding me that it will all be alright. Our first son, James, was born one week before final exams in my last full semester of classes at UWM. He has kept me grounded as I transition from a student to a researcher, making me continuously strive to work smarter so that I will always have time for him. Our second son, Jude, was born three months before I defended my dissertation. His arrival forced into focus what was truly necessary for the completion of this document. And I cannot forget my faithful yellow lab, Ms. Maddy, who has been at my side or asleep at my feet every step along the way.

PREFACE

The work presented in this dissertation stems from my participation in the North American Nanohertz Observatory for Gravitational Waves (NANOGrav) collaboration.

Sections 3.1, 4.1 and 4.2 are based on

Joseph Simon and Sarah Burke-Spolaor, *Constraints on SMBH/Host Co-evolution and Binary Stalling Using Pulsar Timing Arrays*, ApJ **826**, 11 (2016)

Section 3.2 is based on

Joseph Simon, *Velocity Dispersion Function as Proxy for Black-Hole Mass Function: Implications for Pulsar Timing Arrays*, in preparation

Sections 3.3 and 4.3 are based on

Stephen R. Taylor, Joseph Simon, and Laura Sampson, *Constraints On The Dynamical Environments Of Supermassive Black-hole Binaries Using Pulsar-timing Arrays*, PRL, **118**, 181102 (2017)

The results presented in Section 4.2 which utilize the NANOGrav nine-year data set are based on

Zaven Arzoumanian, et al., *The NANOGrav Nine-year Data Set: Limits on the Isotropic Stochastic Gravitational Wave Background*, ApJ **821**, 13 (2016)

Chapter 5 is based on

Joseph Simon and Sarah Burke-Spolaor, *Multi-Messenger Sources for Pulsar Timing Arrays*, in preparation

Chapter 1

Introduction

1.1 The dawn of gravitational-wave astronomy

In 1916, Albert Einstein predicted the existence of gravitational waves: ripples in the curvature of spacetime. Gravitational waves propagate through spacetime, stretching and squeezing the actual fabric of space. They are radiated by massive objects with changing non-spherically symmetric accelerations. However, the influence of gravitational waves was predicted to be so microscopic that Einstein himself declared them ‘un-detectable’. Yet in September of 2015, less than a hundred years after being predicted, the Laser Interferometer Gravitational-Wave Observatory (LIGO), which currently consists of two interferometers in Washington and Louisiana, made the first direct detection of gravitational waves (Abbott et al. 2016). The passing gravitational wave changed the length of each interferometer ‘arm’ – the orthogonal vacuum chambers that house the split laser beams – by less than the size of a proton. The observed gravitational radiation originated from a pair of merging black holes, each with a mass of approximately thirty times the mass of the sun. This discovery marked the dawn of gravitational-wave astronomy.

Just as the electromagnetic spectrum describes a multitude of frequencies of light with corresponding wavelengths and energies, the gravitational-wave spectrum covers frequencies which primarily describe binary systems of celestial compact objects with different orbital periods and masses. Specialized gravitational-wave detectors are needed to cover the full spectrum, in the same way that different telescope apparatus are needed

to observe the sky across the electromagnetic spectrum. Each specialized gravitational-wave detector is only sensitive to a certain range of gravitational-wave frequencies, which is based on the various noise characteristics of each instrument. LIGO is sensitive to gravitational wave frequencies of tens to thousands of hertz. Compact object binaries, e.g. neutron stars and black holes, with total masses ranging from a few to a few hundred times the mass of the sun, emit gravitational waves in this frequency range. However, detection of gravitational waves at other frequencies, which are expected to be emitted by black hole binaries with total masses in the thousands to millions to billions of times the mass of the sun, requires other instruments.

Currently, there are two other types of gravitational wave observatories actively being developed. The Laser Interferometer Space Antenna (LISA) is a joint project between NASA and the European Space Agency to develop and operate a space-based gravitational wave detector which will be sensitive to gravitational wave frequencies in the micro-to milli-hertz range. The LISA detector is of a similar design to the LIGO detectors, but in space the noise characteristics of the interferometer are vastly different. Thus, LISA can detect gravitational waves from more massive black hole binaries than LIGO, which emit gravitational waves at a lower frequency than LIGO's sensitivity range. There is a limit to the size and sensitivity of a space-based interferometer, and other kinds of instruments are needed to access sensitivities at even lower gravitational wave frequencies.

Pulsar Timing Arrays (PTAs) are nano-hertz gravitational wave observatories, which are sensitive to the most massive black hole binaries in the universe. PTAs are not interferometers, but instead rely on accurately monitoring a collection of pulsars, which are a special class of neutron star, spread across our Milky Way galaxy. The distance from Earth to these pulsars is much longer than any interferometer arm, and the light only travels one direction. PTAs are unique instruments with superior sensitivity to supermassive black holes. Gravitational waves from the beginning of the universe are not easily directly detected. Instead, the effect of these primordial gravitational waves can be observed by studying the polarization of light in the cosmic microwave background (CMB). These four main classes of gravitational wave observatories cover the full frequency range of gravitational waves. Fig. 1 shows the relative sensitivities of these instruments across

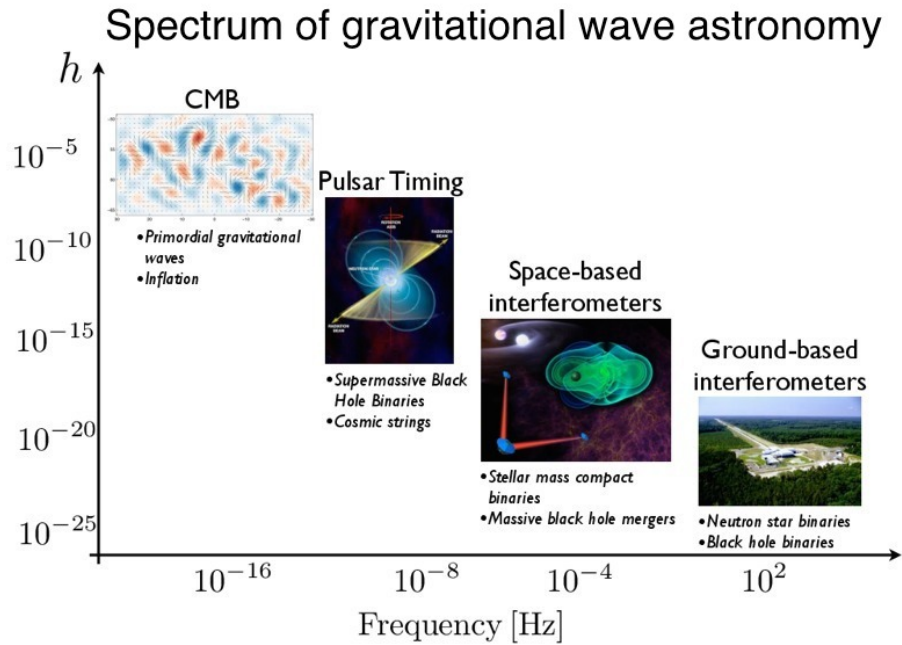


FIGURE 1: The complete spectrum of gravitational wave astronomy is shown in the above figure. LIGO is an example of a ground-based interferometer. LIGO made a direct detection of gravitational waves from two merging black holes in September 2015. LISA is an example of a space-based interferometer. LISA is currently under development and is expected to launch in the early-2030s. NANOGrav, the North American Nanohertz Observatory for Gravitational Waves, is an example of a pulsar timing array. PTAs are sensitive to the most massive black hole binaries in the universe. The effects of the first gravitational waves in the Universe are observable by the effect they have on the polarization of the light in the cosmic microwave background (CMB). BICEP2 (results shown above) is an example of this kind of experiment. The amplitude (h) of the expected gravitational waves that are measurable by each type of observatory are indicated by the vertical placement of the images in the figure, and the expected sources of gravitational waves are listed under each observatory. Credit: NANOGrav

gravitational wave frequency. This dissertation will focus on PTAs and the gravitational radiation from supermassive black holes.

1.2 How do pulsar timing arrays detect gravitational waves?

Pulsars are highly-magnetized, rapidly-rotating neutron stars that emit a constant trail of radio beams. Due to their rotation, this emission appears to be pulsating to a stationary observer, much like the light emitted by a lighthouse. Neutron stars are the remnants of massive stars ($10 - 30 M_{\odot}$), which as a result of their supernovae explosion, condense the core of the star to one of the densest states of matter in the universe. Neutron stars tend to have masses around 1.4 times the mass of the sun with radii of a few tens of kilometers (the approximate size of most large urban cities), which gives them densities where a single teaspoon of neutron star material would weigh a billion tons. For pulsars, the typical rotation speeds are around once per second, but some have been detected spinning as fast as a kitchen blender (Hessels et al. 2006). These are truly exotic objects.

Pulsars appear to come in two distinct varieties. Canonical pulsars are those with periods larger than a few tens of milliseconds, while millisecond pulsars (MSPs) are those with periods less than a few tens of milliseconds. In addition to faster spin periods, MSPs have smaller period derivatives meaning that the rate of change of the period is small. MSPs have been monitored for decades and are incredibly stable. In fact, the precision and stability of the pulses from MSPs rivals those of terrestrial atomic clocks.

Pulsar timing is the observational technique used to determine the rotation parameters of a pulsar. While an individual pulse shape will vary considerably from one pulse to the next, the observed pulsations from several thousand rotations average to form a very stable pulse shape, which is a unique signature for each pulsar. The average pulse profile is used as a model for pulse arrival times for subsequent observations, and deviations from this model, called timing residuals, are tracked over a long period of observations. Each pulsar has a unique set of parameters that will cause deviations over short and long timespans. These include changes in the pulsar clock (i.e., the period, period derivative, and higher order spin rate terms), the proper motion of the pulsar through the galaxy, any binary motion parameters if the pulsar has a companion star (which almost all MSPs

do) and the motion of the Earth around the sun. Appropriately modeling all of these terms for an individual pulsar is a large active area of research, which pulsar timing arrays are built upon.

A passing gravitational wave will cause a time-varying change in the proper distance between the pulsar and the Earth, which will introduce an additional deviation in the observed pulse arrival times. The change in proper distance appears to an observer on the Earth like a change in the pulsar's frequency, or spin period. This apparent change in frequency incorporates information about the gravitational wave amplitude at two locations: where the pulse is emitted (the pulsar) and where it is received (the Earth). The change in frequency due to the gravitational wave amplitude at the Earth will affect each pulsar in a certain way based on the relative distance on the sky between the pulsar and the direction the passing gravitational wave is traveling. The entire array of pulsars has a time-varying change that is correlated due to a gravitational wave, and it is this correlated signature that makes the passing gravitational wave distinguishable from the other timing parameters, which tend to change individual pulsars instead of the entire array.

While the effects of a passing gravitational wave will be present in each individual pulsar's timing residuals – the difference between when each pulse is predicted to arrive, given the known set of parameters of an individual pulsar system, and when the pulse actually arrives – it is only when comparing the timing residuals for a large number of pulsars that the detection of a gravitational wave can confidently be made. Thus, an ideal pulsar timing array would contain many MSPs spread evenly across the sky. In addition to a large number of pulsars, PTAs need long observations since the periods for waves in the nanohertz regime are years to decades. Groups like NANOGrav, along with the other members of the International Pulsar Timing Array, already have more than a decade of PTA observations for a few dozen MSPs and will continue to grow with time (Arzoumanian et al. 2015; Lentati et al. 2015; Shannon et al. 2015).

1.3 What are the gravitational wave sources that pulsar timing arrays can detect?

Prior to LIGO's detection of gravitational waves from a pair of merging black holes, the best evidence for the existence of black holes came from the massive object at the center of our own Milky Way galaxy. By monitoring the orbits of stars in the center of our galaxy, astronomers have estimated that a single object with a mass of over four million solar masses lies at the center of the Milky Way. Extremely massive objects, assumed to be supermassive black holes, appear at the center of almost every other galaxy that has been observed. In the local universe, astronomers have observed a relationship between the masses of these supermassive black holes and the large-scale observables of their host galaxies (e.g., stellar velocity dispersion, galaxy luminosity, galaxy mass, etc.). Figure 2 shows some of these observations and indicates a strong trend line where larger, more massive galaxies host more massive central black holes (Gültekin et al. 2009). Given that the gravitational influence of a central black hole cannot reach the entire galaxy, even for the most massive black holes, it was not expected that the mass of the central black hole would associate so strongly with larger galaxy properties.

The simplest explanation of the trend shown in Figure 2 is a shared growth history, which implies that the seed of a central black hole is present when the galaxy is first formed and grows through cosmic time with the galaxy. Galaxies grow by merging with each other and by gathering gas from the intergalactic medium. If the central black hole was present throughout all of these events, then its properties would be comparable to the larger galaxy properties. Figure 2 also shows that the most massive central black holes appear in elliptical galaxies, which are thought to be the end-products of spiral galaxy mergers. In addition to growth from mergers, supermassive black holes are seen accreting gas onto themselves creating active galactic nuclei (AGN). AGN release energy back into the outer reaches of the galaxy through large jets. This type of feedback process transfers energy from the center of the galaxy to the outer edges and can also regulate the growth of both objects. While there are still open questions around the specifics of how a central supermassive black hole co-evolves with its host galaxy, it is clear from observations that

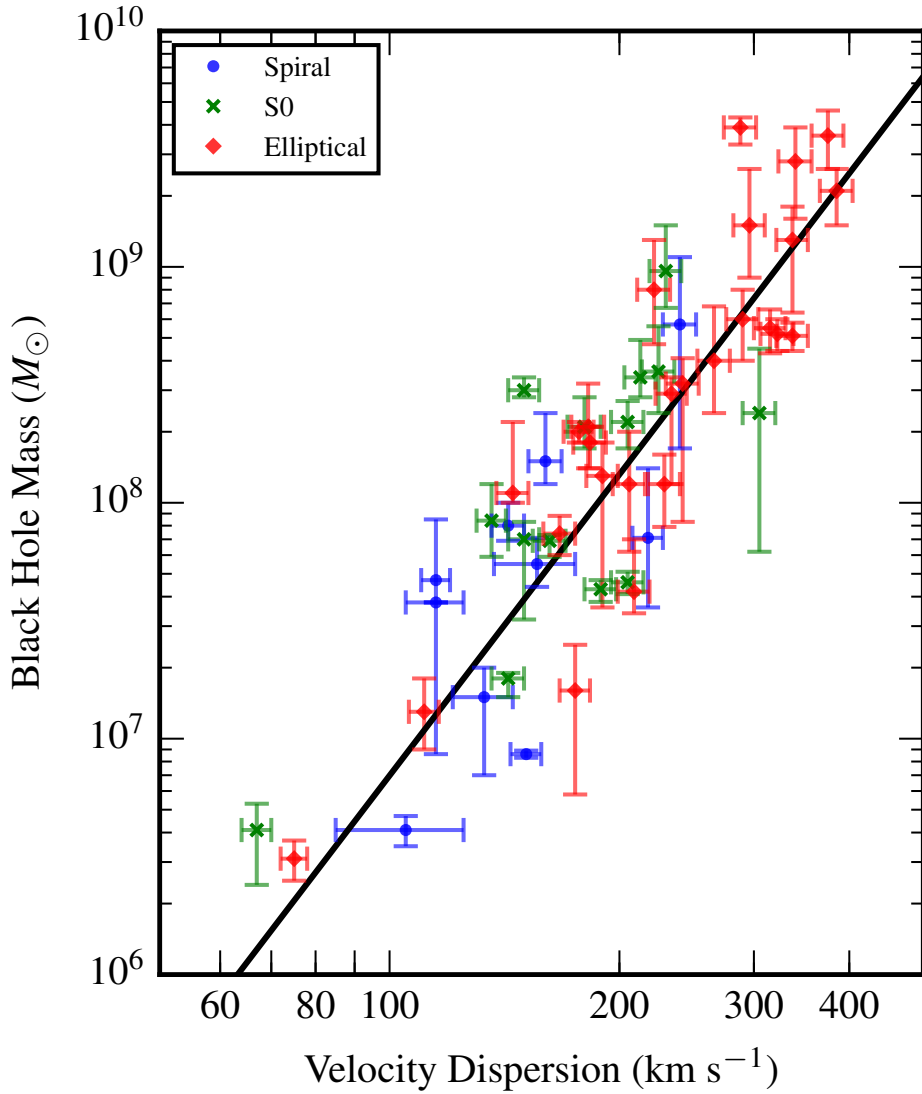


FIGURE 2: This figure shows the observed relation between the mass of a central supermassive black hole, plotted on the vertical axis in solar mass units (M_{\odot}), and a galaxy’s stellar velocity dispersion (σ), plotted on the horizontal axis in kilometers per second. The stellar velocity dispersion is a measure of the variations in stellar velocities in a galaxy and tends to grow with the mass of a galaxy. The plot shows a strong correlation between central supermassive black hole mass and stellar velocity dispersion, which may imply that both the central black hole and the galaxy have grown through cosmic time together with a shared history. The black solid line shows the line of best fit for this relationship. The red diamonds indicate elliptical galaxies, which tend to be more massive and are thought to be the products of spiral galaxy mergers, while the blue circles indicate spiral galaxies, which tend to be less massive. The green marks indicate S0 galaxies, which appear to be the intermediate between spirals and ellipticals. All of the data for the plot above was taken from Gültekin et al. (2009).

this is a key part of galaxy formation and evolution.

Astronomers observe many different types of galaxy interactions. Some of the most violent occur when galaxies collide. While galaxies are diffuse enough that no stars or solar systems run into each other during this process, the large-scale features, like spiral arms and central bulges, get distorted and twist around each other in a long and complicated dance as they merge into a new object. However, this process is estimated to take hundreds of millions of years, so each observation that we take is only a single snapshot. Understanding the galaxy merger process requires combining all of those scattered images into a coherent story, and there are still come gaps in our understanding. The large sample of interacting galaxy pairs implies that most galaxies will undergo numerous merger events in their lifetime. If each galaxy hosts a supermassive black hole and galaxies merge on a regular basis, then it is likely that there exists a population of binary supermassive black holes resulting from the combination of the central regions of merging galaxies. Each binary supermassive black hole will emit strong gravitational radiation when the binary spirals close together and eventually merges into a single supermassive black hole. PTAs are searching for this gravitational radiation.

The emission of strong gravitational radiation, which drives the binary to merge, is the last phase of the merger process. Astronomers observe the beginning stage of the merger, when the two central regions of a merging galaxy combine, but there are other steps between the formation of a central region with two supermassive black holes, where the black holes are separated by large distances, and the emission of strong gravitational waves from the binary, which only happens at much smaller black hole separations. These steps involve interactions between the two supermassive black holes and the stars and gas in the central region of the galaxy and they are not easily observable with telescopes as they typically take place on smaller scales than a telescope can resolve. If these interactions between the the stars and gas and the binary supermassive black hole are strong enough, they have the potential to effect the level of gravitational radiation detected by PTAs. PTAs may be the only tool that can disentangle the various effects that move a binary supermassive black hole from large to small separations.

Unlike the gravitational waves that LIGO has detected, which pass through LIGO's

frequency band in fractions of a second, the gravitational radiation in the PTA band is basically constant over human lifetimes. Thus, all of the gravitational radiation at a specific gravitational wave frequency from all of the binary supermassive black holes spread across the universe combines together to form a constant background. Due to the homogeneity of the universe, the gravitational wave background is different than an individual source, because it is not coming from one direction, but from all directions. PTAs are able to disentangle near-by, loud individual systems from the background, but it is most likely that the first thing detected in the PTA band will be the background. PTA measurements of the gravitational wave background, formed from the population of binary supermassive black holes, will improve our understanding of the co-evolution process of these central black holes and their host galaxies.

1.4 Dissertation Outline

This dissertation describes the creation of a state-of-the-art observational-based simulation framework built to understand the link between PTA data and binary supermassive black holes. In the next chapter, I set out to describe the model parameters that go into building an observational-based simulation for a population of binary supermassive black holes. This requires understanding how to apply the observations of galaxy properties and galaxy mergers, as well as, how to understand the evolutionary processes that drive binary supermassive black holes to radiate gravitational waves in the PTA band. Once all of the model parameters are described and understood, Chapter 3 goes into detail about the observational constraints of various model parameters culminating in predictions on the amplitude of the gravitational wave background. These predictions are then used as a tool to understand and interpret PTA data in Chapter 4. This includes taking PTA limits on the gravitational wave background and placing limits on various model parameters, specifically the parameters that describe the relation shown in Figure 2, known as the $M - \sigma$ relation. Most of the interpretation of PTA limits to date has focused on individual parameters, setting limits one at a time. Some of my recent work has been used to simultaneously fit the density of stars in the central region of a merging galaxy and the initial eccentricity of the binary, which are two parameters that effect the shape

of the gravitational wave background across the PTA frequency band. This is also discussed in Chapter 4. In Chapter 5, we change gears a little bit and move away from the gravitational wave background to explore the potential for incorporating electromagnetic signatures from the active galactic nuclei. These luminous objects are caused by the accretion of matter onto supermassive black holes, which is a process that might be intensified during a galaxy merger. Finally, I present a brief summary of the results of this dissertation and lay-out a series of potential next steps in the final chapter.

Chapter 2

Building A Model for the Gravitational Wave Background from Binary Supermassive Black Holes

This chapter covers a detailed derivation and explanation of the various parameters that are used in modeling a stochastic background of gravitational waves from binary supermassive black holes (SMBHs). As explained in Ch. 1, binary SMBHs are expected to be by-products of galaxy mergers. Thus, observational surveys of galaxy properties can be used as proxies for determining population statistics of binary SMBHs. The following assumes a basic understanding of general relativity and gravitational wave generation, which can be found in Hartle (2003), Creighton & Anderson (2011) and Maggiore (2008). If you would like a more thorough derivation specifically of stochastic backgrounds from gravitational waves, please see Allen (1997) and section 7.8 of Maggiore (2008). See also Phinney (2001) and Jaffe & Backer (2003) for relevant discussions.

2.1 The Gravitational Wave Background

The intensity of a stochastic background of gravitational waves is described by the dimensionless energy spectrum, $\Omega_{GW}(f)$, which is the present-day energy density of gravitational waves carried by the stochastic background, $\rho_{GW}(f)$, per logarithmic frequency interval $d(\ln f) = df/f$ normalized to the critical energy density of the universe, ρ_c .

$$\Omega_{GW}(f) \equiv \frac{1}{\rho_c} \frac{\rho_{GW}(f)}{d(\ln f)}, \quad (2.1.1)$$

where f is the Earth-observed gravitational wave frequency. In an FRW (Friedman-Robertson-Walker) universe,

$$\rho_c = \frac{3H_0^2}{8\pi G}, \quad (2.1.2)$$

where H_0 is Hubble's constant (Ryden 2016). In this work, we use $H_0 = 71 \text{ km s}^{-1} \text{ Mpc}^{-1}$. The characteristic gravitational wave amplitude in a given frequency interval, $h_c(f)$, is related to Ω_{GW} by

$$\Omega_{GW}(f) = \frac{2\pi^2}{3H_0^2} f^2 h_c^2(f). \quad (2.1.3)$$

A stochastic background is produced by the superposition of the radiation from a population of gravitational wave sources. While each individual source is not resolvable, they contribute to the characteristic amplitude of the background by adding a power spectral density $S_h(f)$, characterized by the mean squared strain fluctuations h_s^2 ,

$$h_s^2 = \int df S_h(f). \quad (2.1.4)$$

The observed characteristic squared strain spectrum $h_c^2(f)$ is the integral over all the sources emitting in some strain interval multiplied by the mean squared strain fluctuations of each source.

$$h_c^2(f) = f \int dh h_s^2 \frac{d^2 N}{dh df_r}, \quad (2.1.5)$$

here $d^2 N/dh df_r$ is the number density of sources in a given strain and source rest-frame frequency interval, where $f_r = (1+z)f$ is the frequency of gravitational wave emission in the rest-frame of the source.

We characterize a population of gravitational wave sources by a comoving number density of sources per unit redshift dn/dz . The sources that we are specifically interested

in are a population of binary SMBHs, so the number density of sources can be described as the rate of merger events. The number of merger events in a given redshift bin dz and observational time bin dt is equal to the number of sources in a related strain and rest-frame frequency interval.

$$\frac{d^2N}{dh df_r} = \frac{dn}{dz} dz dt \quad (2.1.6)$$

Thus, the characteristic strain spectrum can be written as

$$h_c^2(f) = f \int dh h_s^2 \frac{dn}{dz} \frac{dz}{dh} \frac{dt}{df_r}. \quad (2.1.7)$$

The number of merger events throughout cosmic history depends on the SMBH masses, meaning

$$\frac{dn}{dz} = \int \int dM_\bullet dq_\bullet \frac{d^3n}{dz dM_\bullet dq_\bullet}. \quad (2.1.8)$$

We define the SMBH masses with the mass of the primary black hole, M_\bullet , and the binary's mass ratio, $q_\bullet = M_{\bullet,2}/M_\bullet$, where we explicitly define $q_\bullet \leq 1$. $d^3n/dz dM_\bullet dq_\bullet$ is the comoving number density per unit redshift, primary black hole mass, and binary mass ratio. Given the discrete nature of the source population, the comoving rate can be expressed as the number of mergers per unit observational time, $d^4N/dz dM_\bullet dq_\bullet dt$:

$$\frac{d^4N}{dz dM_\bullet dq_\bullet dt} = \frac{d^3n}{dz dM_\bullet dq_\bullet} \frac{dV_c}{dz} \frac{dz}{dt_r} \frac{dt_r}{dt}, \quad (2.1.9)$$

where $dt_r/dt = 1/(1+z)$, dV_c/dz is the co-moving volume element and dz/dt_r is the rest-frame time element per redshift. These are as derived by Phinney (2001):

$$\frac{dV_c}{dz} = 4\pi \frac{c D_c^2}{H_0 E(z)}, \quad (2.1.10)$$

$$\frac{dz}{dt_r} = \frac{1}{H_0 (1+z) E(z)}, \quad (2.1.11)$$

where D_c is the co-moving distance to the source defined by

$$D_c = \int_0^z \frac{c}{H_0 E(z')} dz', \quad (2.1.12)$$

$$\text{and } E(z) = \sqrt{\Omega_M (1+z)^3 + \Omega_k (1+z)^2 + \Omega_\Lambda}. \quad (2.1.13)$$

In this work, we use $\Omega_M = 0.27$, $\Omega_\Lambda = 0.73$, and $\Omega_k = 0$. The characteristic strain spectrum can now be written as

$$h_c^2(f) = f \int \int \int dz dM_\bullet dq_\bullet h_s^2 \frac{d^4 N}{dz dM_\bullet dq_\bullet dt} \frac{dt}{df_r}. \quad (2.1.14)$$

Finally, for a convenient notation, we can absorb dt/df_r into the $d^4 N$ term and can translate from the rest-frame frequency, f_r , to the present day, observed frequency of each source, f to end up with an equation for the characteristic strain spectrum which has a simple interpretation: the observed characteristic squared amplitude of the gravitational wave background is given by the integral over all the sources emitting in an observed gravitational wave frequency bin df multiplied by the square strain of each source in that bin.

$$h_c^2(f) = f \int \int \int dz dM_\bullet dq_\bullet h_s^2 \frac{d^4 N}{dz dM_\bullet dq_\bullet df} \quad (2.1.15)$$

Implicit in this derivation is the assumption that the binary formation rate changes slowly relative to the length of a PTA observation and that the binary rapidly enters a regime where it's evolution is dominated by the radiation of gravitational waves, which allows the merger rate to simply be a function of redshift. The dynamics of binary SMBHs is discussed in more depth in Sec. 2.4.

2.2 Determining The Merger Rate

Next, we focus on how the number density of binaries is calculated. The number density of binary SMBHs is a combination of two functions: the SMBH mass function $\Phi_\bullet(z, M_\bullet)$ and the binary merger rate $\mathcal{R}_\bullet(z, M_\bullet, q_\bullet)$.

$$\frac{d^3 n_\bullet}{dz dM_\bullet dq_\bullet} = \Phi_\bullet(z, M_\bullet) \mathcal{R}_\bullet(z, M_\bullet, q_\bullet) \quad (2.2.1)$$

There are currently no direct observational constraints on the demographics of binary SMBHs, so these functions are not explicitly known. Instead, assuming that the number of binaries is directly related to the number of galaxy mergers, the galaxy merger rate is used as a proxy and each galaxy in a merger is populated with a central SMBH using the observed relationship between SMBHs and their host galaxies (e.g., M_\bullet - σ relation,

M_{\bullet} - M_{bulge} relation, etc.). Below, we use (Gal \mapsto \bullet) to denote where the black hole mass - host galaxy relation is applied.

$$\frac{d^3 n_{\bullet}}{dz dM_{\bullet} dq_{\bullet}} = \left| \frac{d^3 n_{\text{Gal}}}{dz dM_{\text{Gal}} dq_{\text{Gal}}} \right|_{\text{Gal} \mapsto \bullet} \quad (2.2.2)$$

The galaxy merger rate, \mathcal{R}_{Gal} , is the redshift-dependent rate at which a galaxy of mass M is involved in a major merger ($q > \frac{1}{4}$) with a second galaxy with mass qM :

$$\mathcal{R}_{\text{Gal}}(z, M, q) = \frac{d^2 n_{\text{Gal}}}{dz dq} = \frac{df_{\text{pair}}(z)}{dq} \frac{1}{\tau_{\text{Gal}}(z, M)} \frac{dt_r}{dz} . \quad (2.2.3)$$

One way to calculate this is by combining the galaxy pair fraction, $f_{\text{pair}}(z)$, and the merger timescale, $\tau(z, M)$. The galaxy pair fraction is an astronomical observable derived by counting the number of dynamically closer pairs of galaxies in a given galaxy survey. The merger timescale, which approximates the dynamical friction timescale for a dynamically bound pair of galaxies, must be determined through simulations. $\tau(z, M)$ is calculated in the rest-frame of the source and converted to a redshift timescale by multiplying τ with the factor dt_r/dz .

2.3 Inferring the Black Hole Mass Function

Now, let us focus on how the SMBH mass function, Φ_{\bullet} , is inferred by populating each galaxy with a central SMBH (Eqn. 2.2.2). One of the results of this work, as seen in Ch. 4, shows that the most important factor in accurately modeling the characteristic strain spectrum of a gravitational wave background is correctly determining the supermassive black hole mass function.

The correlation between the mass of a central supermassive black hole (M_{\bullet}) and a host-galaxy has been generally parameterized as a power-law relation:

$$M_{\bullet} = A \times X^{\beta} \quad (2.3.1)$$

where X is the specific host-galaxy parameter, β is the spectral index of the power-law relation, and A is the scaling factor between the two parameters. For most observed relations, $\beta \approx 1$, which leaves A as the crucial variable to describe the relation. However, in addition to A and β , there is another important measurable quantity, the intrinsic

scatter in M_{\bullet} for a fixed galaxy property (ϵ). The scatter is a useful tool for quantifying how tight a given correlation is and gives a relative measure of value to each category of M_{\bullet} prediction.

Most specific host-galaxy parameters have been observed with large galaxy surveys and have an observed distribution function, $\Phi(z)$, which quantifies the number density of galaxies at a given redshift with a given value of a certain host-galaxy parameter. This observed function gives the underlying redshift distribution of the black hole mass function and when coupled with an appropriate M_{\bullet} to host-galaxy relation gives an inferred black hole mass function.

The M_{\bullet} to host-galaxy relation has been seen across a number of host galaxy parameters, but the most commonly used scaling relations are M_{\bullet} verses stellar velocity dispersion (σ) and M_{\bullet} verses stellar bulge mass (M_{bulge}). The corresponding distribution functions for those galaxy parameters are the velocity dispersion function (VDF) and the galaxy stellar mass function (GSMF), respectively.

Each pair of distribution function and host-galaxy relation includes a specific set of assumptions and has a different set of calculations needs to get from the observed host-galaxy parameter distribution function to the inferred black hole mass function. We explore these two approaches in greater detail below.

2.3.1 GSMF and M_{\bullet} - M_{bulge}

The GSMF is an astronomical observable, and is typically parametrized in terms of a double Schechter function:

$$\begin{aligned} \Phi_{\text{gsmf}}(z, M) &= \left. \frac{dn}{dM} \right|_z \\ &= \frac{e^{-\frac{M}{M^*}}}{M^*} \left[\Phi_1^* \left(\frac{M}{M^*} \right)^{\gamma_1} + \Phi_2^* \left(\frac{M}{M^*} \right)^{\gamma_2} \right]. \end{aligned} \quad (2.3.2)$$

Observations find that quiescent (generally elliptical/early-type) galaxies tend to be more present at higher masses (both for stellar mass and black hole mass) than star-forming (generally spiral/late-type) galaxies (Gültekin et al. 2009; Ilbert et al. 2013). These two distinct galaxy species are also observed to have different internal mass distribution, with the quiescent galaxies having a larger percentage of mass in central bulges than

star-forming galaxies. As such, we classify galaxies as being either quiescent or star-forming, and use accordingly separate Schechter parameters for these when drawing our distributions. Observations of the GSMF bin in redshift, meaning that an observed value of Schechter parameters is only valid over a certain redshift range. We do not assume any kind of clustering effect on mergers, so a quiescent galaxy’s likelihood of merging with another quiescent is only based on the fraction of quiescent galaxies in a given redshift, mass, and mass ratio range. There is some evidence that quiescent galaxy’s are more likely to be found in dense galaxy cluster environments (Baldry et al. 2006), and so there may be a higher probability of a merger containing a quiescent galaxy than what is accounted for in this work.

The fraction of the total stellar mass of the galaxy contained in the bulge, f_{bulge} , is different for each galaxy type. For quiescent galaxies, we assume $f_{\text{bulge}} = 0.9$ for $M > 10^{11}M_{\odot}$, declining log-linearly to $f_{\text{bulge}} = 0.25$ at $M = 10^{10}M_{\odot}$ with an uncertainty of 0.1 dex. These are the dominant producers of gravitational wave power in the PTA band. For star-forming galaxies, which contribute a minor fraction of gravitational wave power to the background regardless of this factor, f_{bulge} is assumed to be 0.25, with an uncertainty of 0.1. This prescription follows that of Sesana (2013b); Ravi et al. (2014) considered a similar prescription with similar results.

The mass of each black hole in a merger is calculated using the M_{\bullet} - M_{bulge} relation that has been observed in the local Universe, which is often displayed in log-space so Eqn. 2.3.1 takes the form

$$\log_{10}M_{\bullet} = \alpha + \beta \log_{10}\left(\frac{M_{\text{bulge}}}{10^{11}M_{\odot}}\right) + \mathcal{N}(\epsilon), \quad (2.3.3)$$

where $M_{\text{bulge}} = f_{\text{bulge}}M$, \mathcal{N} is the normal distribution with a mean of zero and a standard deviation of ϵ , and ϵ is the intrinsic scatter.

2.3.2 VDF and M_{\bullet} - σ

Like the GSMF, the VDF is also an astronomical observable, however, it is typically parameterized in terms of a modified Schechter function:

$$\begin{aligned}\Phi_{\text{vdf}}(z, \sigma) &= \left. \frac{dn}{d\sigma} \right|_z \\ &= \Phi^* e^{(-\frac{\sigma}{\sigma^*})^\beta} \left(\frac{\sigma}{\sigma^*} \right)^\alpha \frac{\beta}{\Gamma(\alpha/\beta)}.\end{aligned}\tag{2.3.4}$$

Similar trends between the relative abundances of quiescent and star-forming galaxies at higher and lower masses found in the GSMF are found at higher and lower σ in VDFs. σ is a spectroscopic measurement, while M is fundamentally a luminosity measurement. They are complementary measurements, with their own types of uncertainty, allowing for two independent probes of the black hole mass function.

The mass of each black hole in the merger is then calculated directly using the M_{\bullet} - σ relation that has been observed in the local Universe, which takes the form

$$\log_{10} M_{\bullet} = \alpha + \beta \log_{10} \left(\frac{\sigma}{200 \text{ km s}^{-1}} \right) + \mathcal{N}(\epsilon),\tag{2.3.5}$$

where \mathcal{N} is the normal distribution with a mean of zero and a standard deviation of ϵ , and ϵ is the intrinsic scatter. One advantage of the VDF is that a direct measurement of σ allows for a single step to calculate M_{\bullet} , bypassing the need to assume something about the relationship between the central bulge and the galaxy like is needed when using the GSMF.

2.4 Binary Black Hole Dynamics

The merger of two galaxies is a messy and complicated process that takes many millions of years to complete.

The evolution of a binary SMBH proceeds in three stages. First, the two galaxy cores plunge towards each other, driven by dynamical friction, and form a common single core. This stage proceeds on a timescale of

$$t_{\text{DF}} \approx \left(\frac{4 \times 10^6 \text{ yr}}{\log N_*} \right) \left(\frac{\sigma}{200 \text{ km s}^{-1}} \right) \left(\frac{r_c}{100 \text{ pc}} \right)^2 \left(\frac{m_{\bullet}}{10^8 M_{\odot}} \right)^{-1}\tag{2.4.1}$$

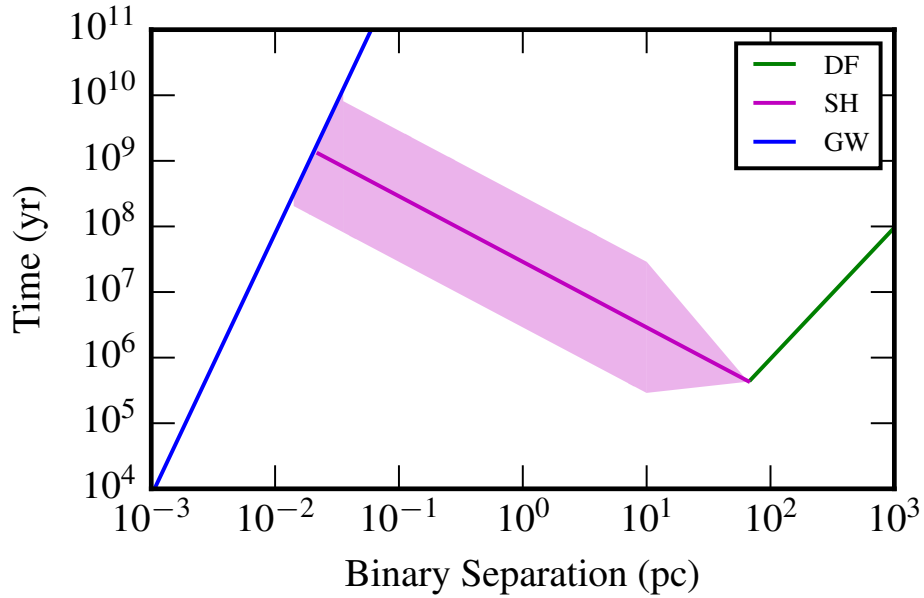


FIGURE 3: The above plot shows the typical timescales involved in the evolution of a binary SMBH for an equal mass binary around $10^8 M_{\odot}$. The binary separation is plotted on the x-axis in parsecs and amount of time that the binary spends at each separation is plotted on the y-axis in years. The green line shows the dynamical friction stage of evolution. The purple solid line shows the typical evolution from stellar scattering from a moderately dense stellar environment for a constantly refilled loss cone. The shaded purple area shows other evolutions for different stellar densities. If the loss cone did not refill, then at around a separation of a parsec the timescale would spike up to the top of the plot, and the binary would stall, never reaching the gravitational radiation dominated evolution. The blue line shows the evolution of the binary due to radiation of gravitational waves. Once the binary reaches the blue evolutionary track, it coalesces into a single object relatively quickly.

where m_{\bullet} is mass of the smaller black hole and the common core has radius r_c , stellar velocity dispersion σ , and contains N_* stars (Begelman et al. 1980). The forces of dynamical friction become inefficient as the binary approaches the so-called hardening radius, defined as (Quinlan 1996)

$$a_h \approx \frac{Gm_{\bullet}}{4\sigma^2} = 2.8 \text{ pc} \left(\frac{\sigma}{200 \text{ km s}^{-1}} \right)^{-2} \left(\frac{m_{\bullet}}{10^8 M_{\odot}} \right). \quad (2.4.2)$$

This is where the second stage of the evolution starts. The third and final stage is driven by gravitational radiation. However, GW emission does not become efficient to drive a binary SMBH to coalescence in less than the age of the Universe until the binary is at a separation of $a \lesssim 0.1 \text{ pc}$. There are various other dynamical mechanisms that may effectively bridge the gap between the hardening radius and the radius needed for a GW-driven prompt coalescence. One of the most commonly cited mechanisms is the interaction of the binary with a core of unbound stars (Quinlan 1996; Sesana et al. 2006). This mechanism is expected to play the largest role in the second phase for galaxy mergers that include elliptical galaxies due to the relatively high density of stars compared to the density of gas in the core of these galaxies (Kormendy et al. 2009). However, other mechanisms such as gas accretion onto one or both SMBHs can play a major role during this stage of evolution (Mayer et al. 2007; Kocsis & Sesana 2011).

A subset of the stars in the core are on trajectories that will carry them past the binary in such a way that the binary will slingshot the star out of the core. The angular momentum transfer from binary to star ‘hardens’ the binary. One of the largest uncertainties regarding the interaction with unbound stars is the relative speed with which the reservoir of unbound stars on trajectories which interact with the binary, called the ‘loss cone’, is refilled. This issue was first discussed in Begelman et al. (1980), and has become known colloquially as the ‘final parsec problem’, since the initial depletion of the reservoir of unbound stars typically occurs when the binary is at parsec separation. Many studies have shown various mechanisms for promptly refilling the loss cone (Khan et al. 2013; Vasiliev et al. 2015). Fig. 3 shows an example of the three stages of binary evolution and includes uncertainties on the second stage. However, the plot does assume that the loss cone refills. If the loss cone never refills then the binary will not coalesce within a Hubble

time. Thus, the binary never enters a GW-dominated energy loss regime, and ‘stalls’ well outside the range of detectability by LISA and PTAs.

2.4.1 Stellar Environments

The distribution of unbound stars is characterized by a density ρ and a velocity dispersion σ . The binary evolution can be expressed as a function of the dimensionless hardening rate H and eccentricity growth rate K (Quinlan 1996):

$$\frac{da}{dt} = \frac{a^2 G \rho}{\sigma} H, \quad (2.4.3)$$

$$\frac{de}{dt} = \frac{a G \rho}{\sigma} H K. \quad (2.4.4)$$

In the above equations, a is the semi-major axis of the binary. When calculating the characteristic strain spectrum (Eqn. 2.1.15) for a stochastic background, we need a form of these equations describing the evolution over orbital frequency, which can then be related to the gravitational wave frequency of the radiation from each binary at a given stage of evolution. Kepler’s Third Law relates the orbital frequency (f_{orb}) and the semi-major axis of any binary using the total mass (M_{tot}) of the binary system.

$$f_{\text{orb}}^2 = \frac{GM_{\text{tot}}}{(2\pi)^2} \frac{1}{a^3}, \quad (2.4.5)$$

Kepler’s Law can be applied in this case because each binary is effectively non-evolving over the timeframe of the PTA observation given the relative time lengths of binary evolution and human lifetimes. The binary can therefore be treated as on a stationary orbit, and so Eqn. 2.4.3 becomes

$$\frac{df_{\text{orb}}}{dt} = \frac{3(2\pi)^{5/6} G^{4/3} \rho H}{2\sigma} M_{\text{tot}}^{1/3} f_{\text{orb}}^{1/3}, \quad (2.4.6)$$

while Eqn. 2.4.4 becomes

$$\frac{de}{df_{\text{orb}}} = \frac{\sqrt{2\pi}}{3} \frac{K}{f_{\text{orb}}}. \quad (2.4.7)$$

Eqn. 2.4.7 is effectively only a function of orbital frequency, which means that the eccentricity at any frequency can be calculated in a straight forward manner given some

initial eccentricity (e_0) at some starting frequency ($f_{\text{orb},0}$).

$$e(f_{\text{orb}}) = \frac{\sqrt{2\pi}K}{3} \ln \left(\frac{f_{\text{orb}}}{f_{\text{orb},0}} \right) + e_0 \quad (2.4.8)$$

In practice, K depends on e among other things. Both H and K are calculated from scattering simulations and will differ depending on the conditions for those simulations. The specific set of simulations for H and K used in this work are discussed in detail in Sec. 3.3.1.

2.4.2 Gravitational Radiation

During the third and final stage of binary evolution, gravitational radiation is the dominant mechanism of energy loss. These binaries are still at cosmological distances, so linearized, plane-wave approximations of gravitational waves are sufficient to describe the effects of gravitational radiation on the system. These equations are given by Peters & Mathews (1963):

$$\begin{aligned} \frac{da}{dt} &= -\frac{64 G^3 M_{\bullet,1} M_{\bullet,2} M_{\text{tot}}}{5 c^5 a^3} (1 - e^2)^{7/2} \left(1 + \frac{73}{24} e^2 + \frac{37}{96} e^4 \right) \\ &= -\frac{64 G^3 M_{\bullet,1} M_{\bullet,2} M_{\text{tot}}}{5 c^5 a^3} F(e) \end{aligned} \quad (2.4.9)$$

$$\frac{de}{dt} = -\frac{304 G^3 M_{\bullet,1} M_{\bullet,2} M_{\text{tot}}}{15 c^5 a^4} (1 - e^2)^{5/2} e \left(1 + \frac{121}{304} e^2 \right). \quad (2.4.10)$$

Again it is useful to use Kepler's Third Law to re-write these in terms of the binary's orbital frequency, so that Eqn. 2.4.9 becomes

$$\frac{df_{\text{orb}}}{dt} = \frac{96}{5} \left(\frac{GM_c}{c^3} \right)^{5/3} (2\pi)^{8/3} f_{\text{orb}}^{11/3} F(e). \quad (2.4.11)$$

and Eqn. 2.4.10 becomes

$$\frac{de}{df_{\text{orb}}} = \frac{19}{18} \frac{1}{f_{\text{orb}}} \frac{(1 - e^2)^{5/2}}{F(e)} e \left(1 + \frac{121}{304} e^2 \right). \quad (2.4.12)$$

Above I have introduced a new parameter called the chirp mass of the binary,

$$M_c = \left(\frac{M_{\bullet,1} M_{\bullet,2}}{M_{\text{tot}}^{1/3}} \right)^{3/5}, \quad (2.4.13)$$

which is a useful parameter to combine the mass terms into a single parameter which scales simply with both gravitational wave strain, which will be shown below in Eqn. 2.5.1, and binary frequency evolution, as shown above.

Eqn. 2.4.12 has a similar functional form for orbital frequency, but is also a complex function of eccentricity. However, as shown in Enoki & Nagashima (2007), it is still possible to calculate the eccentricity at any frequency given some initial eccentricity (e_0) at some starting frequency ($f_{\text{orb},0}$):

$$\frac{f_{\text{orb}}}{f_{\text{orb},0}} = \left\{ \frac{1 - e_0^2}{1 - e^2} \left(\frac{e}{e_0} \right)^{\frac{12}{19}} \left[\frac{1 + \frac{121}{304}e^2}{1 + \frac{121}{304}e_0^2} \right]^{\frac{870}{2299}} \right\}^{-3/2}. \quad (2.4.14)$$

Yunes et al. (2009) find an accurate fit ($< 1\%$ fitting error) for the numerical solution to $e(f_{\text{orb}})$ derived from Eqn. 2.4.14, which is the functional use that we desire from the above formula. The fit takes the form of the following fraction (Eqn. 3.12 in Yunes et al. (2009)):

$$e(f_{\text{orb}}) = \frac{16.83 - 3.814\beta^{0.3858}}{16.04 + 8.1\beta^{1.637}}, \quad (2.4.15)$$

where $\beta = \chi^{2/3}/\sigma_0(e_0)$, $\chi = f_{\text{orb}}/f_{\text{orb},0}$, and

$$\sigma_0(e_0) = \frac{e_0^{12/19}}{1 - e_0^2} \left(1 + \frac{121}{304}e_0^2 \right)^{\frac{870}{2299}}. \quad (2.4.16)$$

More will be discussed about the implementation of these formulae to calculate the strain spectra in Sec. 2.6, but first we will review the amplitude of gravitational wave emission from an individual binary SMBH.

2.4.3 Binary Stalling

If the loss cone does not refill efficiently, then the binary will ‘stall.’ Different amounts of stalling will impact GW signals in different ways. Let’s recall that the number density of galaxy mergers is being used as a proxy for the number density of binary SMBH mergers (Eqn. 2.2.2). This assumes that the binary SMBH merger happens promptly following the galaxy merger. Practically this means that the redshift unit used to describe d^3n_\bullet is assumed to be equivalent to the redshift unit describing d^3n_{Gal} . Once an appreciable amount of cosmological time passes as the binary travels between the first stage of evolution, where the galaxy merger rate is calculated, and the final stage of evolution, where the galaxy is emitting gravitational radiation in the pulsar timing array band, then we need to adjust the model by accounting for this time.

Let us introduce a variable T_{stall} , the time between the galaxy merger and the binary SMBH entering the PTA band. This stalling timescale variable creates a redshift offset between the galaxy merger and the binary SMBH's PTA band gravitational wave emission. This is incorporated into Eqn. 2.2.2 by setting z_1 as the redshift of the galaxy merger, and z_2 as the redshift at which the binary is emitting in the PTA band. T_{stall} is the proper time between z_1 and z_2 . The total effect of T_{stall} on the number of mergers per observational time is incorporated in the cosmological parameters in Eqn. 2.1.9 by moving the binary closer since $z_2 < z_1$.

$$\frac{d^4 N}{dz_2 dM_{\bullet} dq_{\bullet} dt} = \left| \frac{d^3 n_{\text{Gal}}}{dz_1 dM_{\text{Gal}} dq_{\text{Gal}}} \right|_{\text{Gal} \mapsto \bullet} \frac{dV_c}{dz_2} \frac{dz_2}{dt}. \quad (2.4.17)$$

The effect of T_{stall} on the predictions from this model are discussed in Sec. ??.

2.5 Gravitational Radiation from Binary SMBH

The polarization and sky-averaged strain from one circular binary system is (Peters & Mathews 1963; Thorne 1987)

$$h_s = \sqrt{\frac{32}{5}} \left(\frac{GM_c}{c^3} \right)^{5/3} \frac{c}{D_c} (2\pi f_{\text{orb}})^{2/3}, \quad (2.5.1)$$

where M_c is the chirp mass of the binary (described in Eqn. 2.4.13), D_c is the proper distance to the binary (Eqn. 2.1.12), and f_{orb} is the orbital frequency of the system. The rest-frame frequency of the gravitational waves emitted by a circular system, f_r , are at the second harmonic, $f_r = n f_{\text{orb}}$ where $n = 2$.

An eccentric source emits gravitational waves across many harmonics depending on the value of the eccentricity. The more eccentric a binary, the more harmonics it emits in. The strain emitted at each harmonic is then

$$h_{n,s}(e) = \sqrt{\frac{32}{5}} \left(\frac{GM_c}{c^3} \right)^{5/3} \frac{c}{D_c} \left(2\pi \frac{f_r}{n} \right)^{2/3} g(n, e), \quad (2.5.2)$$

where $g(n, e)$ is the gravitational wave frequency distribution function (Peters & Mathews 1963)

$$g(n, e) \equiv \frac{n^4}{32} \left\{ \left[J_{n-2}(ne) - 2eJ_{n-1}(ne) + \frac{2}{n}J_n(ne) + 2eJ_{n+1}(ne) - J_{n+2}(ne) \right]^2 + (1 - e^2) [J_{n-2}(ne) - 2eJ_n(ne) + J_{n+2}(ne)]^2 + \frac{4}{3n^2} [J_n(ne)]^2 \right\}. \quad (2.5.3)$$

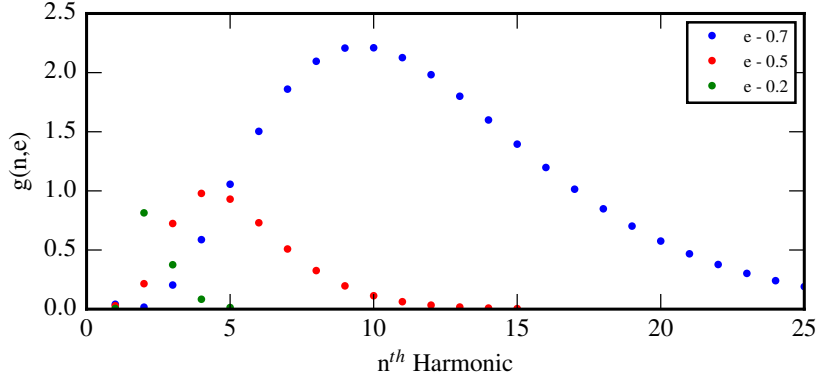


FIGURE 4: The above plot shows the relative power radiated into the n th harmonic for three specific values of eccentricity, $e = 0.2, 0.5$, and 0.7 . For a circular source ($e = 0$) all of the power is radiated at $n = 2$.

Above, J_n represents the n th-order Bessel function. Figure 4 illustrates how larger values of eccentricity radiate power across cumulatively more GW frequency harmonics.

The attenuation factor, $F(e)$, that first appears in Eqn. 2.4.9, accounts for all of the radiation emitted by an eccentric binary across all harmonics. It is related to $g(n, e)$ like so (Peters & Mathews 1963):

$$\sum_{n=1}^{\infty} g(n, e) = F(e) . \quad (2.5.4)$$

For circular sources, $F(e) = 1$. As the eccentricity of a source increases, it not only radiates gravitational waves at higher harmonics, but due to that extra radiation, the source evolves more rapidly. However, the radiation of gravitational waves works quickly to circularize the binary, as seen in Eqn. 2.4.10. The implications of these dynamical effects for our models are discussed in depth in Sec. 3.3.1.

2.6 The PTA Strain Spectrum

Now we return to the $h_c^2(f)$ function (Eqn. 2.1.15) and incorporate all of the ingredients explained in Sections 2.2 - 2.5 into a useable model for the characteristic strain power spectrum. First, let us focus just on the $d^4 N_{\bullet} / dz dM_{\bullet} dq_{\bullet} df$ term and incorporate that with Eqn. 2.1.9 to get

$$\frac{d^4 N_{\bullet}}{dz dM_{\bullet} dq_{\bullet} df} = \frac{d^3 n_{\bullet}}{dz dM_{\bullet} dq_{\bullet}} \frac{dV_c}{dz} \frac{dz}{dt} \frac{dt}{df} . \quad (2.6.1)$$

Incorporating Eqn. 2.2.1 with the change from black hole parameters to galaxy merger parameters in Eqn. 2.2.2, the $d^4 N_\bullet$ term expands to become

$$\frac{d^4 N_\bullet}{dz dM_\bullet dq_\bullet df} = |\Phi_{\text{Gal}}(z, M_{\text{Gal}}) \mathcal{R}_{\text{Gal}}(z, M_{\text{Gal}}, q_{\text{Gal}})|_{\text{Gal} \mapsto \bullet} \frac{dV_c}{dz} \frac{dz}{dt} \frac{dt}{df}. \quad (2.6.2)$$

Then we insert the definition of \mathcal{R}_{Gal} from Eqn. 2.2.3 to obtain

$$\frac{d^4 N_\bullet}{dz dM_\bullet dq_\bullet df} = \left| \Phi_{\text{Gal}} \frac{df_{\text{pair}}}{dq} \frac{1}{\tau_{\text{Gal}}} \frac{dt_r}{dz} \right|_{\text{Gal} \mapsto \bullet} \frac{dV_c}{dz} \frac{dz}{dt} \frac{dt}{df} \quad (2.6.3)$$

Finally, since dz/dt is a cosmological term that does not depend on the mass of either the galaxy or the black hole, and we are holding to the assumption that the galaxy merger and the black hole merger occur at the same redshift, we can move to cancel those terms leaving

$$\frac{d^4 N_\bullet}{dz dM_\bullet dq_\bullet df} = \left| \frac{\Phi_{\text{Gal}}}{\tau_{\text{Gal}}} \frac{df_{\text{pair}}}{dq} \right|_{\text{Gal} \mapsto \bullet} \frac{dV_c}{dz} \frac{dt_r}{df}. \quad (2.6.4)$$

This will hold for any appropriate combination of Φ_{Gal} and black hole – host galaxy relation ($\text{Gal} \mapsto \bullet$), two of which are described in detail in Sec. 2.3.

When Eqn. 2.6.4 is inserted into Eqn. 2.1.15 the variables of integration can be changed to galaxy merger parameters since the only parameters that need black hole masses are h_s^2 and dt_r/df which gives rise to the complete $h_c^2(f)$ formula:

$$h_c^2(f) = f \left| \int \int \int dz dM_{\text{Gal}} dq_{\text{Gal}} \frac{\Phi_{\text{Gal}}}{\tau_{\text{Gal}}} \frac{df_{\text{pair}}}{dq} \right|_{\text{Gal} \mapsto \bullet} \frac{dV_c}{dz} \frac{dt_r}{df} h_s^2. \quad (2.6.5)$$

In the above equation, the only two terms that contain factors of f are dt_r/df and h_s^2 . For the simplest case, a circular binary with gravitational radiation dominated evolution, we see from Eqn. 2.4.11 and Eqn. 2.5.1 that there is a simple power-law expression for $h_c^2(f)$ which can be described by a dimensionless amplitude A_{yr} (Jenet et al. 2006):

$$h_c^2(f) = A_{\text{yr}}^2 \left(\frac{f}{f_{\text{yr}}} \right)^{-\frac{4}{3}}. \quad (2.6.6)$$

The reference frequency of $f = f_{\text{yr}} = \text{yr}^{-1}$ is chosen as a common convention. However, it has the benefit of being at a high enough frequency that even if the binary enters the PTA band under some other kind of evolutionary forces and/or is eccentric, by the time the typical binary reaches a gravitational wave frequency of $f = \text{yr}^{-1}$ it may have circularized due to gravitational radiation and its evolution will be dominated by that

same radiation. This allows A_{yr} to be used as a high frequency anchor when exploring different parameters of binary dynamics.

PTA constraints are therefore often quoted as an upper limit on A_{yr} using this basic $h_c \propto f^{-2/3}$ model for the expected stochastic background in the PTA band, extrapolated from the actual limit at some lower frequency around $f = 2/T_{\text{obs}}$. For this reason, models of the background often quote predictions on A_{yr} . By combining Eqns. 2.6.6 & 2.6.5, predictions for A_{yr} can be calculated by:

$$A_{\text{yr}}^2 = \left| \int \int \int dz dM_{\text{Gal}} dq_{\text{Gal}} \frac{\Phi_{\text{Gal}}}{\tau_{\text{Gal}}} \frac{df_{\text{pair}}}{dq} \Big|_{\text{Gal} \mapsto \bullet} \frac{dV_c}{dz} \left(\frac{dt_r}{d(\ln) f} h_s^2 \right) \Big|_{f_{\text{yr}}} \right|. \quad (2.6.7)$$

To obtain the full strain spectra, one can simply integrate Eqn. 2.6.5 across the desired observed frequency band. However, numerical integration will produce the mean strain distribution, but fails to capture the effects of cosmic variance. In our Universe, the stochastic background is made up of discrete sources, where the actual number of sources present in a given redshift range $(z, z + \Delta z)$, galaxy mass range $(M_{\text{Gal}}, M_{\text{Gal}} + \Delta M_{\text{Gal}})$, galaxy mass ratio range $(q_{\text{Gal}}, q_{\text{Gal}} + \Delta q_{\text{Gal}})$, and observational gravitational wave frequency range, $(f, f + \Delta f)$ is

$$N_{\Delta z \Delta M_{\text{Gal}} \Delta q_{\text{Gal}} \Delta f} = \text{Pois} \left(\frac{d^4 N_{\bullet}}{dz dM_{\bullet} dq_{\bullet} df} \Delta z \Delta M_{\text{Gal}} \Delta q_{\text{Gal}} \Delta f \right), \quad (2.6.8)$$

where $\text{Pois}(x)$ indicates a Poisson sampled distribution. Thus, the characteristic strain spectra from a discretely sampled distribution in some frequency bin with central value f_c is equal to the weighted quadrature sum of the strain from the sources emitting in that frequency bin, or

$$h_c^2(f_c) = \sum_{i=1}^{N_{\Delta f}} h_{i,s}^2(f_i) \frac{f_i}{\Delta f}, \quad (2.6.9)$$

where $f_i \in (f_c - (\Delta f/2), f_c + (\Delta f/2))$.

For an individual PTA, the frequency range and spectral resolution are set by the total observation time and the cadence of observations. The spectral resolution, or frequency bin size, is the inverse of the total observation length. This is also a good approximation for the minimum value of the frequency range that a PTA observation is sensitive to.

$$\Delta f = f_{\text{min}} = \frac{1}{T_{\text{obs}}} \quad (2.6.10)$$

The maximum frequency is the inverse of the cadence of observations. On average, most PTA have a cadence of three weeks, which puts $f_{\max} \approx 100$ nHz. While current PTA observational lengths are slightly over a decade ($f_{\min} \sim 2 - 3$ nHz), in order to project out over the next decade of PTA observations, it is common to set $f_{\min} \sim 1 - 2$ nHz.

The calculation of Eqn. 2.6.9 becomes slightly more complicated when considering eccentric binaries and/or non-gravitational radiation evolution. When dealing with non-gravitational radiation evolution, the form of dt_r/df changes accordingly. For example, when the evolution of the binary is dominated by interactions with an unbound stellar core, Eqn. 2.4.6 is used which makes $h_c^2(f) \propto f$. For some population of binaries which are dominated by stellar interactions at low-frequency (larger separations), there will be some bend frequency (f_{bend}) where the effects of stellar slingshots and gravitational radiation are equal, and above that frequency gravitational radiation will be the dominant evolutionary mechanism. The bend frequency gets its name from the fact that the characteristic strain changes from being proportional to a positive power of the frequency at lower frequencies to being proportional to a negative power of the frequency at higher frequencies, which will create an actual bend in the strain spectra. A simple approximation for a spectral shape of this kind is derived in Sampson et al. (2015). When a model is incorporating multiple evolutionary forces, the dt_r/df for each is calculated for each binary, and the mechanism that gives the smallest value is the dominant mechanism. Since dt_r/df is typically also a function of other galaxy parameters, the dominant mechanism may be different for all binaries across the studied frequency range.

For eccentric sources, one not only needs to keep track of the frequency evolution of the binary, but also the eccentricity evolution of the binary. Additional complications arise when trying to use a formula like Eqn. 2.6.11 because each binary is now no longer emitting at a single gravitational wave frequency. While there have been some derivations of a straight forward formula to describe the characteristic strain spectra from a population of eccentric binaries (see (Enoki & Nagashima 2007; Huerta et al. 2015)), in this work we have chosen to instead obtain $h_c^2(f)$ without using numeric approximations. To calculate an eccentric characteristic strain spectra, we first replace the observed gravitational wave frequency range in Eqn. 2.6.8, with an orbital frequency range ($f_{\text{orb}}, f_{\text{orb}} + \Delta f_{\text{orb}}$). Then

we calculate the the strain distribution for each source from Eqn. 2.5.2. Finally, we calculate the characteristic strain from the quadrature sum of each part of the strain from any binary that is emitting in a given frequency bin.

$$h_c^2(f_c) = \sum_i h_{i,n,s}^2(e, n_i f_{\text{orb}}) \frac{n_i f_{\text{orb}}}{\Delta f}, \quad (2.6.11)$$

where $n_i f_{\text{orb}} \in (f_c - (\Delta f/2), f_c + (\Delta f/2))$.

In Chapter 3, predictions made using the models described above will be discussed, and Chapter 4 will show how these predictions and models can be used to interpret PTA data.

Chapter 3

Predictions for the Gravitational Wave Background from Binary Supermassive Black Holes

This chapter builds on the models derived in Chapter 2 and lays out various predictions for both the amplitude and the spectral shape of the gravitational wave background in the PTA band. We start by investigating a fiducial model, which combines galaxy stellar mass functions (Φ_{gsmf}), galaxy merger rates (\mathcal{R}_{Gal}), and the M_{\bullet} - M_{bulge} relation. Next, we compare those predictions to ones made using a velocity dispersion function (Φ_{vdf}) and the M_{\bullet} - σ relation in an attempt to more accurately predict the SMBH mass function (Φ_{\bullet} , described in Sec. 2.3). Finally, models for stellar scattering and eccentricity are used to create a full distribution of spectra shapes for use in Chapter 4.

3.1 Predictions for A_{yr} : Fiducial Model

Sesana (2013b) presented the first systematic investigation of the gravitational wave background using a similar method as the one derived in Chapter 2 to calculate A_{yr} and utilizing the mean values of many different observations. The following section seeks to update that investigation in a complimentary way to what was done in Ravi et al. (2015), which used fewer, but more complete observations and focused closely on the uncertainties in the galaxy merger rate as well as other uncertainties inherent to the specific observations

used to determine the GSMF. This work attempts to find a balance between these two approaches, using multiple current and complete observations, while also attempting to parse which details are more relevant to A_{yr} predictions.

3.1.1 \mathcal{R}_{Gal} Constraints

The observed galaxy merger rate (\mathcal{R}_{Gal}) is a combination of the observed galaxy pair fraction f_{pair} , and an analytically calculated merger timescale τ_{Gal} (see Eqn. 2.2.3). The galaxy pair fraction, f_{pair} is fairly well constrained in the local universe ($z \sim 0.1$), but is less constrained with increasing redshift (Keenan et al. 2014). For our purposes, f_{pair} is well described as a simple redshift power-law,

$$f_{\text{pair}} = A_{\text{pair}} (1 + z)^m, \quad (3.1.1)$$

where A_{pair} is the value of f_{pair} at $z \approx 0$, and m describes the redshift evolution of f_{pair} out to $z \sim 2 - 3$, where f_{pair} is expected to peak and turn-over for the most massive galaxies, which we are interested in (Conselice 2014). This work utilizes the galaxy pair fraction from the GAMA survey (Robotham et al. 2014) and the combined value resulting from analysis of the RCS1, UKIDSS, and 2MASS surveys (Keenan et al. 2014). While these two papers agree on the pair fraction in the local universe ($z \sim 0.1$), they differ by a factor of two on the redshift dependence of the pair fraction, with Keenan et al. (2014) showing a lower value.

Neither observation goes to high enough redshift to observe a turn-over, so we do not include one. By keeping the slopes of f_{pair} constant out to $z = 3$, we find that the values of f_{pair} reached are approximately at both the high and low ends of predictions, respectively (Conselice 2014). While both Sesana (2013b) and Ravi et al. (2015) use the f_{pair} measurement from Xu et al. (2012), it is not used in this work because the authors of Robotham et al. (2014) note that a local pair fraction observation from Xu et al. (2012), which sets both the low fraction at $z = 0$ and the high slope of the redshift dependence of the presented f_{pair} relation, has been shown to be unrealistic. The revised measurement of Xu et al. (2012) calculated in Robotham et al. (2014) is consistent with Robotham et al. (2014), so we do not feel any additional f_{pair} measurement is required to give a robust prediction.

For self-consistent comparisons, recent observations of the galaxy pair fraction use one of two formulas for τ_{Gal} (Lotz et al. 2011; Kitzbichler & White 2008), which differ by a factor of two. The Kitzbichler & White (2008) timescale is a lower limit for the galaxy merger timescale because it is derived by a dark matter halo merger timescale from the Millennium Simulation. Lotz et al. (2011) calculates τ_{Gal} from a set of hydrodynamical simulations, which incorporates gas and dust into the galaxy merger, unlike Kitzbichler & White (2008). Xu et al. (2012) combined the mass and redshift dependence from Kitzbichler & White (2008) with the results from Lotz et al. (2011) to give a description of the major-merger timescale for $z < 1$

$$\tau_{\text{Gal}} = 0.3 \text{ Gyr} \left(\frac{M}{10^{10.7} \text{ M}_{\odot}} \right)^{-0.3} \left(1 + \frac{z}{8} \right), \quad (3.1.2)$$

which is combined with the pair fractions described above to give the two different galaxy merger rates used in this work. Since one of the main focuses of this work is the effects of observable galaxy evolution parameters on the gravitational wave background, we do not investigate different formulations of tau. However, in Ravi et al. (2015) the removal of the mass and redshift dependence in τ_{Gal} was found to produce a slightly higher value for A_{yr} .

3.1.2 Φ_{gsmf} Observations

The total GSMF is fairly well-constrained by observation out to $z = 1.5$ (Tomczak et al. 2014; Ilbert et al. 2013), however there is still debate over how the total GSMF breaks down by galaxy type (star-forming vs. quiescent). Quiescent galaxies dominate the gravitational radiation that PTAs are sensitive to because they host larger black holes than star-forming galaxies. Therefore, the break-down of galaxy type as a function of mass and redshift has a large impact on the overall signal. This work does not assume any kind of clustering effect on mergers, so a quiescent galaxy's likelihood of merging with another quiescent is only based on the fraction of quiescent galaxies in a given redshift, mass, and mass ratio range. Ravi et al. (2015) shows that while there is some possibility for contamination of colour-selected GSMFs, the overall effect on the amplitude of the GWB is negligible compared to other contributions.

This work utilizes the GSMF measured by the CANDELS/ZFOURGE survey (Tomczak et al. 2014), and the full UltraVISTA survey (Ilbert et al. 2013) for $z > 0.2$. The ZFOURGE survey provided the deepest GSMF measurements at the time of this work (Tomczak et al. 2014), while the UltraVISTA survey covers a wide field, so they complement each other well. These two surveys show consistent results with the updated GSMF from Muzzin et al. (2013) used by Ravi et al. (2015). For $z < 0.2$, the SDSS/GALEX observations of the local universe GSMF from Moustakas et al. (2013) are utilized.

3.1.3 The M_{\bullet} - M_{bulge} Relation

In the past few years, some observations have found a steeper relationship than previously observed for the correlation between bulge mass and the mass of the resident SMBH. The steeper values are largely due to the recent measurements of the high-mass end of M_{bulge} , which in turn house the most massive SMBHs that will contribute to the gravitational wave signal in the PTA band (Scott et al. 2013; Kormendy & Ho 2013; McConnell & Ma 2013). As we aim to predict the most realistic stochastic background signal as relevant to PTAs, our simulation only considers the M_{\bullet} - M_{bulge} relations that include these massive galaxy measurements. Figure 5 shows a demonstration of how the parameters of Eqn. 2.3.3 vary with the inclusion or exclusion of measurements at the high-mass end, and various other considerations. It is unclear whether a single power-law best describes this relationship over the full mass range (Graham 2016), but it appears to be sufficient for the most massive systems, and so in this work we do not consider the broken power-law prescriptions in Scott et al. (2013). Additionally, we note that the high mass relation in Scott et al. (2013) is almost identical to the relation in Kormendy & Ho (2013).

Measurements of the M_{\bullet} - M_{bulge} relation also include ϵ , the “intrinsic scatter”, which is the natural scatter of individual galaxies around the trend line described by α and β in Eqn. 2.3.3, as discussed in Section 2.3. This parameter plays a critical role in A_{yr} predictions as a way accounting for the outliers in the distribution. The galaxies containing over-massive black holes will contribute more to the gravitational wave signal in the PTA band than other galaxies of similar mass and thus are a necessary inclusion

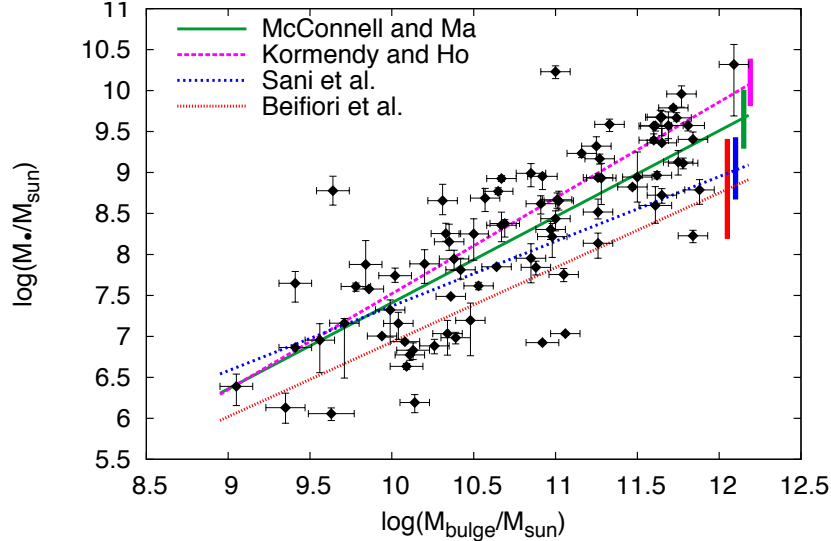


FIGURE 5: Demonstration of the variation in M_{\bullet} - M_{bulge} correlations in the literature. The intrinsic scatter parameter, ϵ , is shown as a \pm vertical bar for each relation. The points are given by the measurements in the review of Kormendy & Ho (2013). The differences in α and β measurements depend on a number of effects including: 1) mass range considered; 2) inclusion of pseudobulges/other subsample effects; and 3) how bulge mass is determined (dynamical vs. stellar luminosity). The major difference between the KH13/MM13 fit and the Sani et al. (2011)/Beifiori et al. (2012) fits is the inclusion of new measurements of galaxies at the highest-mass end for KH13/MM13.

into any prediction of A_{yr} .

3.1.4 A_{yr} Distribution: Fiducial Model

Combining all of the observational constraints from Sections 3.1.1 - 3.1.3 into the model from Eqn. 2.6.7, we calculate a range of predictions for A_{yr} . The inputs are allowed to vary within the reported observational errors for each combination of GSMF, f_{pair} , and M_{\bullet} - M_{bulge} relation described above. Each combination is run 500 times for a total of 4000 predictions of A_{yr} . Figure 6 shows a plot of this distribution for major-mergers, $q_{\text{Gal}} > 1/4$, of primary galaxies with a stellar mass in the range $M_{\text{Gal}} \in (10^{10}M_{\odot} - 10^{12}M_{\odot})$ and lying in the redshift range $z < 3$. Additionally, we include the predictions from Sesana (2013b) and Ravi et al. (2015), and find that all ranges on A_{yr} are similar. Fig 6 also indicates where recent PTA upper limits fall in respect to this model's predictions. The most recently published upper limit at the time of this work comes from 11 years of data taken by the Parkes Pulsar Timing Array (PPTA Shannon et al. 2015), which quotes

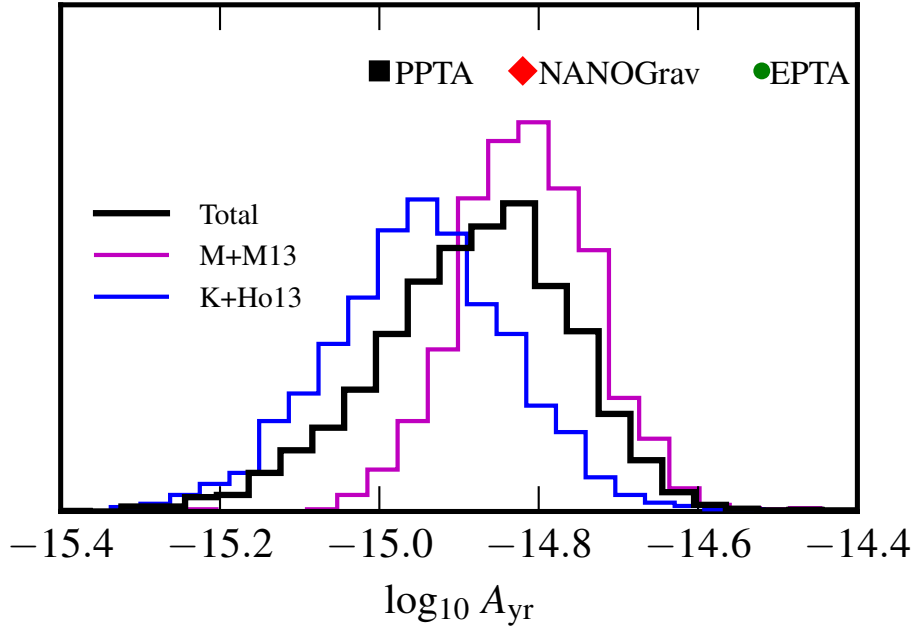


FIGURE 6: The solid black line is the total distribution calculated using the errors reported with the measurements we have chosen to use, described in Sections 3.1.1 - 3.1.3. Additionally, the total distribution is broken down by M_{\bullet} - M_{bulge} relation, with Kormendy & Ho (2013) shown in magenta, which is understood to predict higher values of A_{yr} because the measurement is weighted strongly by large mass observations, as seen in Fig. 5, while McConnell & Ma (2013) shown in blue is not, and thus creates slightly smaller black hole masses. The breadth of the distributions results from the observed variance in our input parameters, and also from the fact that we use multiple formulations for the GSMF and f_{pair} . The most recent upper limits from each PTA are shown as points directly above the distribution of A_{yr} .

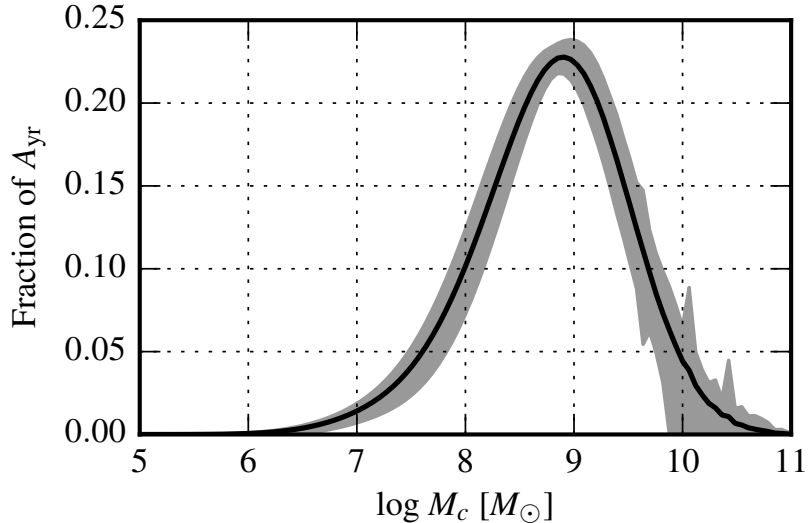


FIGURE 7: Each prediction of A_{yr} is the quadrature sum of many binaries. The solid black line shows the fraction of A_{yr} that comes from binaries with a given M_c . The gray region shows the one sigma error region for this distribution. The value of A_{yr} is dominated by binaries with $M_c > 10^8 M_\odot$, as expected.

an upper limit on A_{yr} of 1.0×10^{-15} . The North American Nanohertz Observatory for Gravitational Waves (NANOGrav) has released nine years of data which produce an upper limit of $A_{\text{yr}} < 1.5 \times 10^{-15}$ (Arzoumanian et al. 2015), and the European Pulsar Timing Array (EPTA) quoted an upper limit of A_{yr} of 3.0×10^{-15} (Lentati et al. 2015). PTA upper limits are typically shown to “rule out” some portion of the predicted range on A_{yr} . However, it is often unclear what that means in terms of limits on the input SMBH evolution parameters. Below, we aim to provide clarity by determining how, and how much, each parameter effects the resulting prediction of A_{yr} .

As expected for each prediction, A_{yr} is dominated by binary sources with chirp masses larger than $10^8 M_\odot$ as seen in Figure 7, which shows how the cumulative contribution to A_{yr} from increasing chirp masses. Figure 8 shows that the majority of the signal is produced at $z \lesssim 1.5$, also as expected, but there is a lot of variance at lower redshift, which is discussed further in Section 3.1.5. Figure 8a shows the contribution from binaries at different redshifts for both GSMFs used in this paper. While the general trend is the same for each, the differences in them directly follow the way that each GSMF handles the abundance of massive early-type galaxies, specifically between $0.5 < z < 1.5$.

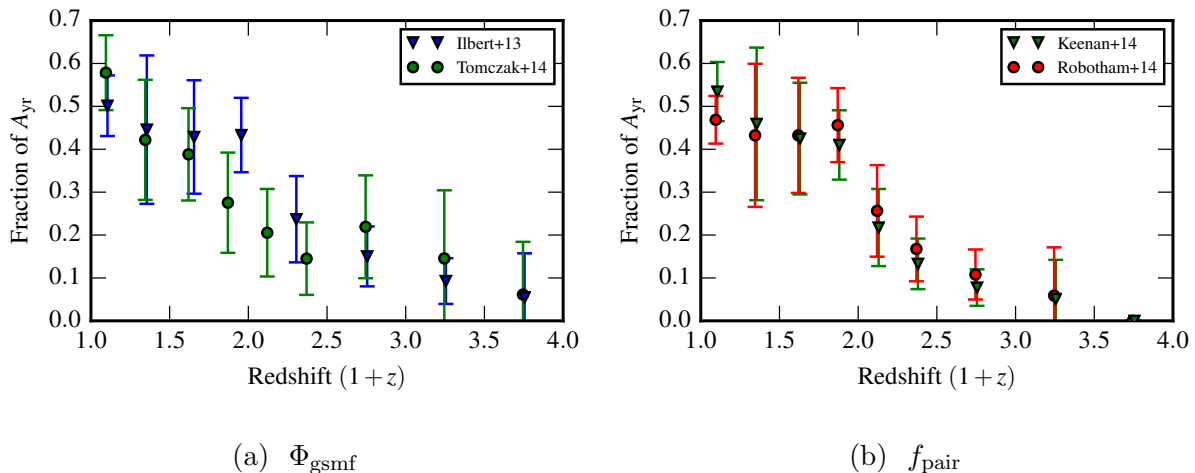


FIGURE 8: The above plots show the fractional contributions to A_{yr} , plotted in Figure 6, as a function of redshift for various observational measurements. (a) The redshift distribution of A_{yr} of the GSMF from Ilbert et al. (2013) is plotted as blue triangle points, while the GSMF from Tomczak et al. (2014) is plotted as the green circular points. The GSMF provides the mass distribution of galaxies as a function of redshift, and thus affects how each redshift bin will contribute to the total value A_{yr} . Both GSMFs are plotted with error bars, which indicate the root-mean-squared value from all simulation runs. While the majority of the contribution to A_{yr} comes from binaries at $z \lesssim 1.5$, there is a large amount of variance which is dominated by the uncertainty in the amount of massive galaxies in this redshift range. We discuss the relative contributions from variance in the GSMFs on the variance of A_{yr} predictions in Section 3.1.5. (b) f_{pair} is the fraction of galaxy pairs in a certain mass, redshift and mass ratio range that are undergoing a merger. This parameter sets the number of sources that will be contributing to A_{yr} . While both measurements have the same value at $z = 0$, the redshift dependencies vary by a factor of two. The higher slope f_{pair} from Robotham et al. (2014), shown above in red circles, contributes less at lower redshifts than the lower slope f_{pair} from Keenan et al. (2014), shown above in green triangles, which is directly related to the number of binaries contributing to A_{yr} at higher redshifts.

At higher redshifts the amount of signal is dominated by the total number of binaries, which is set in part by f_{pair} . The effect of different f_{pair} on the redshift distribution of the contribution to A_{yr} is shown in Figure 8b. While both values of f_{pair} used in this paper have the same value at $z = 0$, the redshift dependencies vary by a factor of two. However, as described in Section 3.1.1, the two values trace the upper and lower ends of predictions for f_{pair} at high redshift. An interesting feature of Figure 8b is that the higher slope f_{pair} from Robotham et al. (2014) contributes less at lower redshifts than the lower slope f_{pair} from Keenan et al. (2014). This trend is directly related to the number of binaries contributing to A_{yr} at higher redshifts.

3.1.5 Relative effects of GSMF, f_{pair} , and M_{\bullet} - M_{bulge} on A_{yr}

Each parameter in Eqn. 2.6.7 that has an observational constraint also has an associated error. These errors obviously effect the variance in the final strain spectrum prediction. In Fig. 9, we show the 1σ range of predictions for A_{yr} given by each combination of observational parameters. The percentage contribution to the total error is broken down for each parameter in a given combination, and shown underneath the predicted range of A_{yr} . Below, we discuss the breakdown of the errors in *individual observational parameters* impact on the final range of A_{yr} .

Given that $A_{\text{yr}}^2 \propto M_c^{5/3}$, the parameters which affect the binary chirp mass should have substantial impact on the prediction of A_{yr}^2 (Sesana & Vecchio 2010). Accordingly, we find the M_{\bullet} - M_{bulge} relation sets the mean value for A_{yr}^2 predictions, as can be seen by the breakdown in Figure 6. This is the relation that provides the translation from galaxy population to BH mass and therefore sets the mean value of the M_c distribution.

The GSMF plays a large role in determining the variance of a certain prediction. All mass functions used in this paper are parametrized using a double Schechter function (Eqn 2.3.2) for $z < 1.5$, so there are a lot observed parameters included in each calculation. Looking at each Schechter parameter and the error bars associated with it reveals that uncertainty in M^* has the largest effect A_{yr}^2 predictions, contributing 45% of the GSMF error for both observations used in this paper. M^* is the mass at which the Schechter function transitions between the high-mass exponential decay and the lower-mass slopes

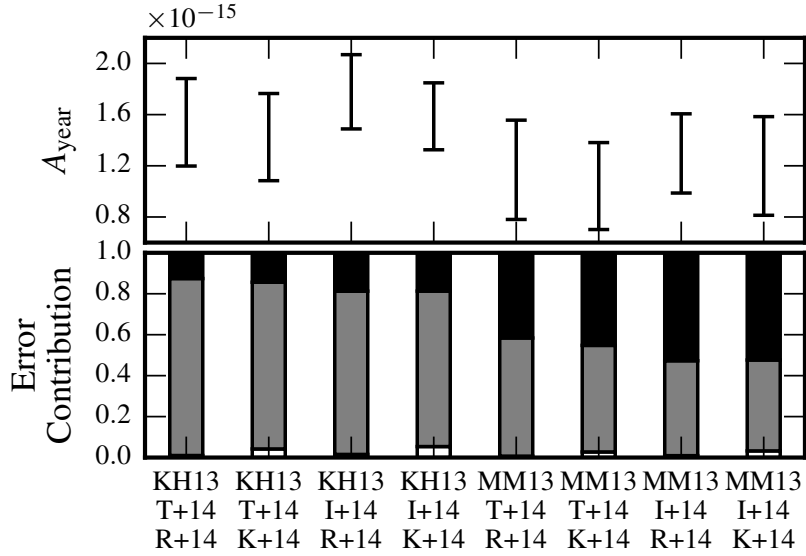


FIGURE 9: In the top portion of this graph, the error bars show the one sigma region of predictions for A_{yr} for each combination of galaxy evolution parameters used in the model. The bottom portion of the graph shows the stacked error contributions from each parameter. The black region is from the M_{\bullet} - M_{bulge} relation, while the gray region is from the GSMF, and the white region is from f_{pair} . The label on each combination shows which measurement was used: KH13 - (Kormendy & Ho 2013), MM13 - (McConnell & Ma 2013), T+14 - (Tomczak et al. 2014), I+14 - (Ilbert et al. 2013), R+14 - (Robotham et al. 2014), K+14 - (Keenan et al. 2014). Clearly the error from the GSMF measurements dominate the error budget of each prediction, followed by the error from the M_{\bullet} - M_{bulge} relation. The errors in f_{pair} are minimal as there is barely a hint of white in each stacker bar graph. The implications of this plot are discussed in Section 3.1.5.

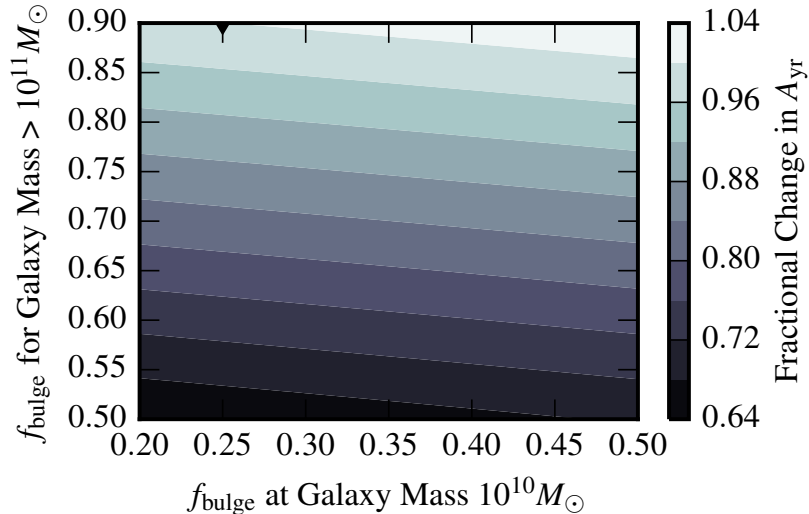


FIGURE 10: f_{bulge} describes the fraction of a galaxy’s total mass contained in the central bulge. This parameter is used to estimate a black hole’s mass using the host galaxy’s total stellar mass. For quiescent galaxies there are two parameters used to set f_{bulge} , a value for massive galaxies, $M > 10^{11}M_{\odot}$, which is plotted on the y-axis, and a value for the less massive galaxies, $M = 10^{10}M_{\odot}$, which is plotted on the x-axis. For galaxies with masses between $M_{\text{Gal}} \in (10^{10}M_{\odot} - 10^{11}M_{\odot})$, f_{bulge} is assumed to follow a log-linear line between the set values. Both of these values were allowed to vary and the resulting fractional change in A_{yr} is shown on the z-axis in color. In this paper we use the values (0.25, 0.9), which is the point used for comparison in the fractional change shown in the color bar. Overall there is not a strong dependence on A_{yr} from the parameterization of f_{bulge} .

α_1 and α_2 . The error from the local GSMF, $z < 0.2$ (Moustakas et al. 2013), is minimal at 2% of the GSMF error, but the next redshift bin, $0.2 < z < 0.5$, in both GSMF observations used in this paper provides the largest influence by redshift on GSMF error contribution to A_{yr}^2 at 55% for Tomczak et al. (2014) and 72% for Ilbert et al. (2013).

The host galaxy’s mass is used to estimate each black hole’s mass using f_{bulge} . f_{bulge} for quiescent galaxies is described with two values, one that sets the fraction of mass in the central bulge for massive galaxies, $M_{\text{Gal}} > 10^{11}M_{\odot}$, and one that sets the fraction of mass in the central bulge for galaxies with stellar masses of $10^{10}M_{\odot}$. Given the dominance of the signal from binaries with chirp masses above 10^8M_{\odot} , the effect of the quiescent galaxy’s f_{bulge} on A_{yr} was calculated. Fig. 10 demonstrates the dependence of A_{yr} on f_{bulge} for quiescent galaxies, making it clear that there is not a strong dependence (less than a factor of $\sim \sqrt{2}$).

The pair fraction, f_{pair} , has the least impact on A_{yr}^2 . Although the parameter itself has a large range, it only impacts the number of sources ($A_{\text{yr}}^2 \propto N$), rather than the masses of those sources. The error in f_{pair} primarily comes from the error on the local universe measurement of the f_{pair} rather than m . The significant difference in errors between the two observations of this parameter comes from their fact that their reported errors on the local universe measurement are a factor of two different, however, the measurement they make is within 5% of each other, so overall this parameter is fairly well constrained.

3.1.6 Conclusions: Fiducial Model

The A_{yr} predictions plotted in Fig. 6 are consistent with other published predictions which use similar methods, and appear in some tension with published PTA limits. We will discuss this tension in Chapter 4. The mean and range of the predictions are dominated by two parameters: the M_{\bullet} - M_{bulge} relation, which appears to be the dominant parameter in setting the mean value for a set of predictions, and the uncertainty in the GSMF, which dominates the range covered by a given prediction. The GSMF and the M_{\bullet} - M_{bulge} relation are combined and used as a proxy for the underlying supermassive black hole mass function (Φ_{\bullet}), given that the uncertainty in these proxies dominate the uncertainty in predictions, it is worth exploring if there are other proxies that could be used to predict Φ_{\bullet} . This would not only be a useful exercise for comparing results, but if the uncertainty could be significantly lowered that would open up the possibility to place constraints on τ (Eqn. 3.1.2), which is currently not well constrained.

3.2 Predictions for A_{yr} : Φ_{vdf} vs. Φ_{gsmf}

Recent work has increasingly suggested that the stellar velocity dispersion (σ) is a more fundamental property of a galaxy than the stellar mass (Wake et al. 2012; van den Bosch 2016), and that the M_{\bullet} - M_{bulge} relation is just an extension of the more fundamental M_{\bullet} - σ relation. Given the desire, described above, to find another method to infer the supermassive black hole function (Φ_{\bullet}), this led me to pursue a way of describing the number density of galaxy's directly by σ . In addition to using a different black hole mass - host galaxy relation, using σ instead of M_{bulge} minimizes the number of steps

and assumptions used by removing the need for estimating the fraction of stellar mass contained in the bulge (f_{bulge}).

Inserting σ for M_{Gal} and M_{bulge} in the $h_c(f)$ calculation is fairly straight forward. Φ_{vdf} is swapped for Φ_{gsmf} and the M_{\bullet} - σ relation is swapped for the M_{\bullet} - M_{bulge} relation. \mathcal{R}_{Gal} is almost identical, except that τ_{Gal} as constructed in Eqn. 3.1.2 has a dependence on M_{Gal} , which is no longer a parameter being drawn for each galaxy, so we remove the galaxy mass dependence and use a simpler form of τ_{Gal} which only has the redshift dependence. To make sure that the new predictions are comparable to the fiducial model, the range of parameter space covered by the number density integral should be similar. To cover a similar range of galaxies, we use $\sigma \in (100, 500)$, which is comparable to $M_{\text{Gal}} \in (10^{10}M_{\odot}, 10^{12}M_{\odot})$.

The definition of a major merger was based on M_{Gal} , so the range of q_{Gal} needs to be replaced by a comparable range in q_{σ} . To do this we use the virial theorem assuming that stellar mass is proportional to dynamical mass (Taylor et al. 2010):

$$\sigma \propto \sqrt{\frac{M_{\text{Gal}}}{r_e}}, \quad (3.2.1)$$

where r_e is the effective radii, which can be related to the galaxy stellar mass by $r_e \propto M_{\text{Gal}}^{0.56}$ (Shen et al. 2003), combining these together, one gets

$$\sigma \propto M_{\text{Gal}}^{0.22}. \quad (3.2.2)$$

Therefore $1 > q_{\text{Gal}} > 1/4$ translates to $1 > q_{\sigma} > 0.74$.

3.2.1 Φ_{vdf} Constraints

The extensive study of the local velocity dispersion function (VDF) in the SDSS, which covers $z < 0.3$, gives a strong anchor from which to extend a study of VDFs to higher redshifts (Sheth et al. 2003; Bernardi et al. 2010). However, measuring a complete VDF using dynamical measurements would require an extremely large spectroscopic survey, which does not exist at the moment. Instead, work has been done to estimate an inferred velocity dispersion (σ_{inf}) for galaxies at higher redshift ($0.3 < z < 1.5$) using a combination of stellar mass (M_{Gal}), effective radii (r_e), and Sèrsic index (n). The inferred velocity dispersion is then related to the intrinsic velocity dispersion (σ) using the SDSS sample

of galaxies. This method was first attempted by Bezanson et al. (2011), which calculated the evolution of the total VDF out to $z \sim 1.5$.

For $z < 0.3$, this work uses the VDFs reported in Bernardi et al. (2010). Sheth et al. (2003) made the first measurement of the quiescent VDF in the SDSS fitting it with a modified Schechter function (shown in Eqn. 2.3.4). Other quiescent and total VDFs have been fit using the same functional form. For $0.3 < z < 1.5$, this work utilizes the VDF from Bezanson et al. (2012), which takes the same method from Bezanson et al. (2011) and using a large uniform sample makes morphological cuts to create a separate VDF for quiescent and star-forming galaxies. These cuts are similar to the morphological cuts made in GSMFs, however σ_{inf} does not appear to have the same level of confusion with morphological color-selection as M_{Gal} , as discussed for GSMFs. Like σ , σ_{inf} is a better predictor of quiescence than stellar mass (Wake et al. 2012; Bezanson et al. 2012). While quiescent VDFs take the form of a modified Schechter function, star-forming VDFs in Bezanson et al. (2012) stay mostly flat in log-log space before falling off quickly at high σ_{inf} , so a double power-law is used to describe those functions (Bezanson 2016).

3.2.2 The M_{\bullet} - σ Relation

Similar to the M_{\bullet} - M_{bulge} relation, recent observations have found more black holes at the most massive end of this relation (McConnell & Ma 2013). However, unlike the M_{\bullet} - M_{bulge} relation, the M_{\bullet} - σ relation does differ with galaxy morphology. There is a different fit for the quiescent and star-forming galaxy populations, while both take the same form (Eqn. 2.3.5). In this work, the M_{\bullet} - σ relations from McConnell & Ma (2013) are paired with the Φ_{vdf} from Bezanson et al. (2012). The predictions from this pairing are discussed in Sec. 3.2.4, where they are also contrasted with the Φ_{gsmf} and M_{\bullet} - M_{bulge} predictions described in Section 3.1.4.

3.2.3 Variations in M_{\bullet} from M_{\bullet} - σ vs. M_{\bullet} - M_{bulge}

Before comparing the predictions of A_{yr} from Φ_{vdf} and Φ_{gsmf} , let us first look at comparisons for predicting M_{\bullet} in quiescent galaxies from M_{\bullet} - M_{bulge} vs. M_{\bullet} - σ . Using the measured scaling relation for M_{Gal} and σ for the SDSS from (Zahid et al. 2016) and the

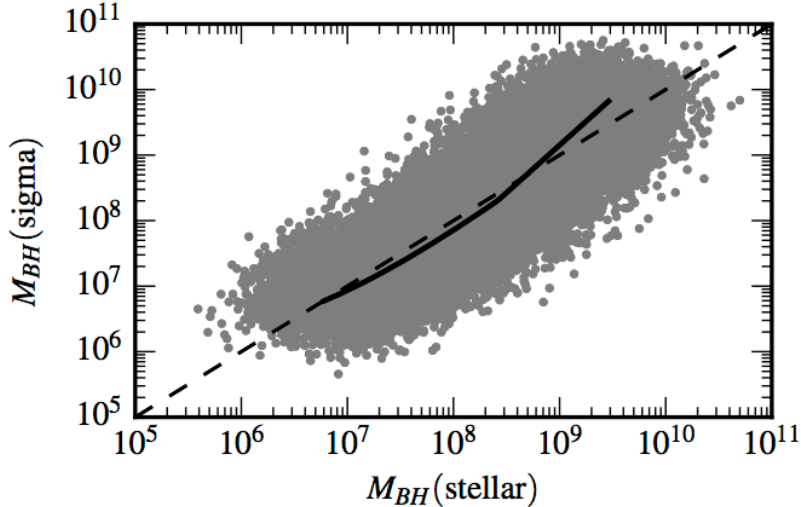


FIGURE 11: A direct comparison between using M_{Gal} and σ as a proxy for the mass of a quiescent galaxy’s central SMBH is plotted above, with the M_{\bullet} from M_{Gal} on the x-axis and from σ on the y-axis. The dotted line follows a direct one-to-one matching, and the solid line shows the mean value of comparison. While the scatter around the relationship is large, due to the intrinsic scatter ϵ in both the M_{\bullet} - M_{bulge} and the M_{\bullet} - σ relations, the values given are relatively consistent with each other. For massive black holes ($> 10^9 M_{\odot}$) σ appears to infer slightly larger M_{\bullet} than M_{Gal} .

measured M_{\bullet} - M_{bulge} and quiescent M_{\bullet} - σ from McConnell & Ma (2013), we can create a direct comparison of these two methods, derived from observational constraints.

Figure 11 shows the results for quiescent galaxies with $M_{\text{Gal}} \in (10^9 M_{\odot} - 10^{12} M_{\odot})$. The intrinsic scatter ϵ in both the M_{\bullet} - M_{bulge} and M_{\bullet} - σ relation translates to a large scatter in M_{\bullet} predictions, but the mean relation shows each method giving approximately the same result. They diverge slightly from each other for high black hole masses ($M_{\bullet} > 10^9 M_{\odot}$) with the M_{\bullet} inferred using the M_{\bullet} - σ relation being larger than that given by the M_{\bullet} - M_{bulge} relation. At high M_{\bullet} for the M_{Gal} method, f_{bulge} is set to 0.9, and a similar trend is seen if f_{bulge} is set to 1 for $M_{\text{Gal}} > 10^{11} M_{\odot}$. The implications of this are seen and discussed further in the rest of this section.

3.2.4 A_{yr} Distribution: Comparing Φ_{vdf} vs. Φ_{gsmf}

Predictions for A_{yr} are calculated from Eqn. 2.6.7 in a similar matter to that described in Sec. 3.1.4, but Φ_{vdf} , as described in Section 3.2.1, is swapped for Φ_{gsmf} and the M_{\bullet} - σ relation, as described in Section 3.2.2 is swapped for the M_{\bullet} - M_{bulge} relation. The predicted

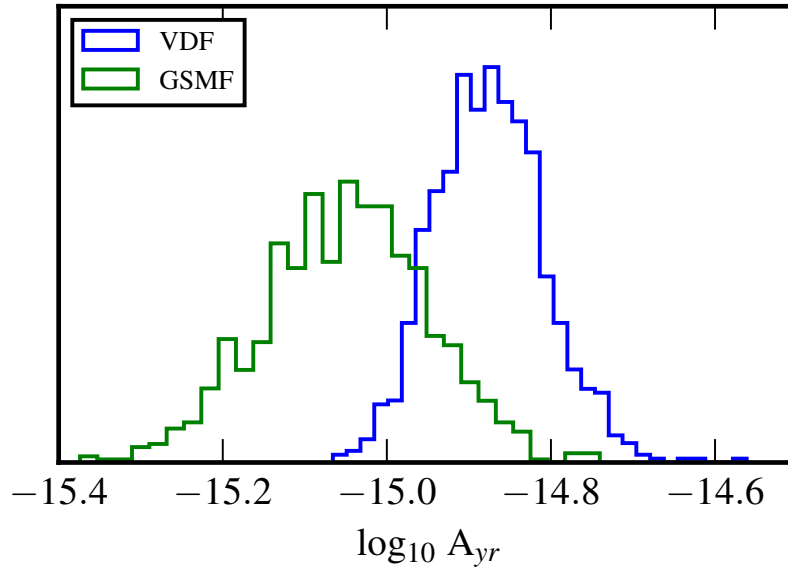


FIGURE 12: The blue line is the A_{yr} distribution prediction using a velocity dispersion function (VDF) as a proxy for the black hole mass function, described above in the first portion of Section 3.2. The green line is an A_{yr} distribution prediction from the fiducial model which uses a galaxy stellar mass function (GSMF), described in Section 3.1. Both distributions utilize a modified τ_{Gal} so that the results are comparable, and both use black hole mass - host galaxy relations measured from the same set of observations, McConnell & Ma (2013). The A_{yr} distribution from the VDF is larger than that from the GSMF, which is consistent with the direct comparison shown in Figure 11 and can be understood as the effect of higher mass binaries. This effect is seen more clearly in the A_{yr} vs. M_c plot (Figure 13).

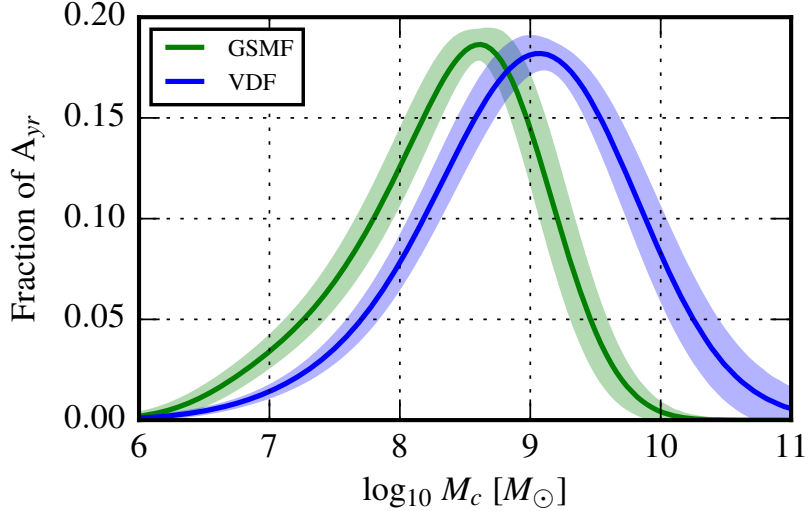


FIGURE 13: The solid green lines shows the fraction of A_{yr} that comes from binaries with increasing chirp mass, M_c , for the A_{yr} predictions that use galaxy stellar mass functions (GSMFs), while the solid blue line shows the fraction of A_{yr} for the predictions that use velocity dispersion functions (VDFs). The shaded regions around the solid lines indicate the one sigma error region for these distributions. The green line is comparable to the distribution shown for the fiducial model in Figure 7. The VDF distribution is roughly 0.5 dex larger, on average, with a slightly smaller offset at lower chirp mass and a slightly larger offset at high chirp mass. This trend may follow from the larger black hole masses predicted using σ in comparison to M_{Gal} .

distribution of A_{yr} is plotted in Figure 12 along side a distribution of A_{yr} from the fiducial model, which uses the GSMF from Ilbert et al. (2013), f_{bulge} from Robotham et al. (2014), and M_{\bullet} - M_{bulge} from McConnell & Ma (2013), the one difference in this distribution from the fiducial model is the use of a modified τ_{Gal} to not skew the comparison results. The GSMF distribution is slightly lower than what was shown in the fiducial model (compare the green distribution in Figure 12 to the [MM13, I+14, R+14] column of Figure 9), which is expected with the removal of the mass dependence in τ_{Gal} . The VDF distribution predicts a higher value of A_{yr} , which may be caused by higher mass black holes being predicted by σ relative to M_{bulge} , as seen in Figure 11.

The difference in predicted black hole masses is most clearly seen in Figure 13, which plots the fractional contribution to A_{yr} as a function of binary SMBH chirp mass, M_c . The VDF distribution, shown in blue, is about 0.5 dex higher than the GSMF distribution, shown in green. As discussed in Section 3.1.5, $A_{\text{yr}} \propto N^{1/2} M_c^{5/3}$. For an average M_c

increase of 0.5 dex, the predicted A_{yr} should increase by 0.4 dex if nothing else changes, since an average M_c increase will automatically decrease the average N given that more massive binaries evolve faster ($dt/df \propto M_c^{-5/3}$, see Eqn. 2.4.11). However, Figure 12 only shows a mean A_{yr} increase of 0.2 dex between the VDF and the GSMF distributions. Thus, the VDF predictions must have an even smaller mean number of sources at each chirp mass, particularly the most massive, than the GSMF. Fewer sources in the VDF distribution must then come from the different black hole mass function proxies used in each prediction, Φ_{vdf} or Φ_{gsmf} .

In conclusion, σ predicts a gravitational wave background of comparable amplitude to that from M_{Gal} . However, the population of binary SMBHs predicted using σ is built up from fewer, more massive sources than the M_{Gal} predictions. While these populations might look similar when comparing A_{yr} predictions, the underlying demographics should reveal different strain spectra across the PTA band. The assumptions of stochasticity and isotropy of the background require a large number of sources at relatively equal strain evenly distributed across the sky.

3.2.5 Spectral Shape: Comparing Φ_{vdf} vs. Φ_{gsmf}

Full strain spectra are obtained using Equation 2.6.9. The biggest difference between creating a full spectra from a population and predicting A_{yr} values is that the full spectra is made up of discrete sources, which allows the results to incorporate cosmic variance, the sample variance from different realizations of the Universe. The effects of cosmic variance have been shown to cause the stochastic background to deviate from the expected power law behavior (Equation 2.6.6) at high frequencies ($f \gtrsim 20$ nHz) (Sesana et al. 2008; Roebber et al. 2016). Figure 14 contains the mean and standard deviation from 500 realizations of the strain spectra predicted using VDFs (shown in blue) and GSMFs (shown in green). The dashed line shows the expected power-law behavior of a stochastic background from binaries which have evolution dominated by gravitational radiation. The GSMF spectra deviates from that power law around the expected frequency range due to cosmic variance. The VDF spectra deviates from the power law model at a much lower frequency of $f \sim 3$ nHz.

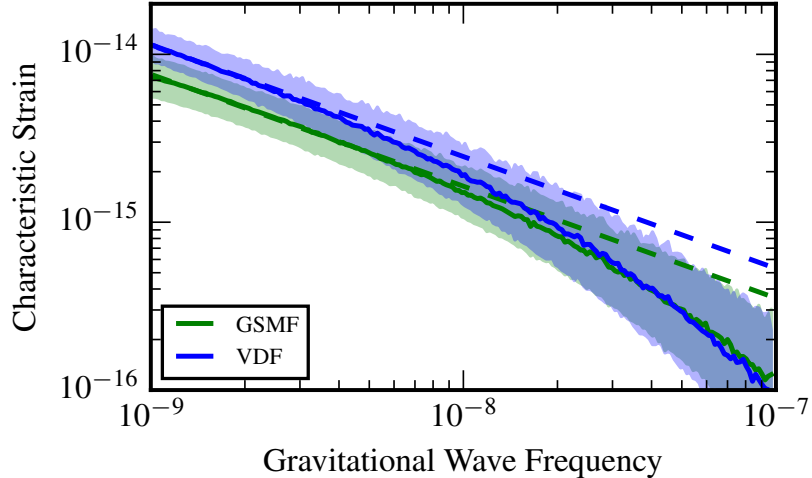


FIGURE 14: The green solid line shows the mean strain spectra from 500 realizations of the binary SMBH population using GSMFs, while the blue solid line shows the mean strain spectra for a population made using VDFs. The shaded region around both solid lines represent the one sigma error bar region associated with the mean spectra values. The dashed lines show the expected power-law behavior for a stochastic background (Equation 2.6.6). The GSMF populations deviate from the power law at high frequencies ($f \gtrsim 10$ nHz) as expected, while the VDF populations start to deviate at a lower frequency of $f \sim 3$ nHz. This deviation is due to cosmic variance.

The populations used to make Figure 14 assume that gravitational radiation will be the dominant form of binary evolution across the entire PTA band. However, as discussed in Section 2.4, there is the possibility that different mechanisms of binary evolution may be dominant at the lower end of the PTA band. Given that the VDF populations show strong cosmic variance at lower frequencies than previously thought, we produce another set of populations that are evolved in a dense distribution of unbound stars in the galactic cores. The evolutionary equations for this type of binary dynamics are described in Section 2.4.1, with ρ set to $1000M_{\odot} \text{ pc}^{-3}$, which is a relatively high value that is expected to cause a low-frequency turnover in the spectrum in the PTA band. Figure 15 shows the resulting spectra from these populations. The frequency where the spectra turns over for the VDF population is at a lower frequency than that in the GSMF population, which again matches the expectation for the binary’s hosting more massive black holes, as the bend frequency (the frequency where the turn-over occurs) is inversely proportional to the total mass of the binary (Sampson et al. 2015). The level of cosmic variance in the

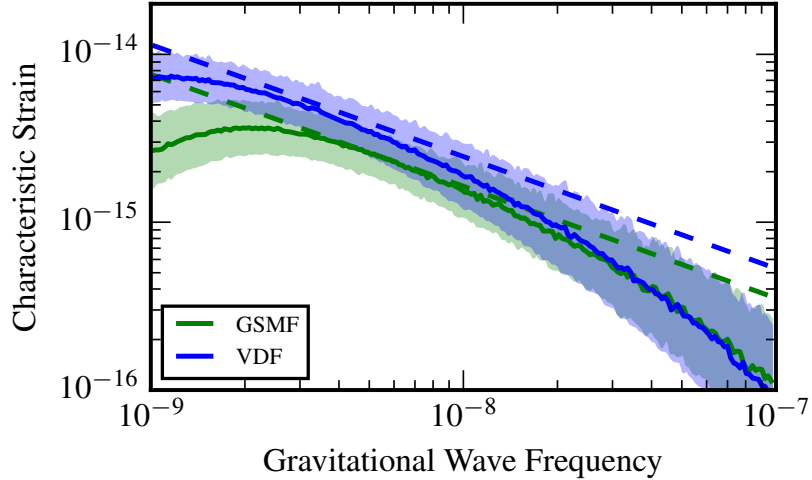


FIGURE 15: Again the green and blue solid lines show the mean strain spectra from 500 realizations of the binary SMBH population using GSMFs and VDFs, respectively. The difference between these spectra and those seen in Figure 14 is the incorporation of a low-frequency turn-over due to interactions with a dense ($\rho = 1000M_{\odot} \text{ pc}^{-3}$) distribution of unbound stars in the galaxy core (discussed in Section 2.4.1). The shaded regions represent the one sigma error regions associated with the mean spectra values, and the dashed lines are the same as those in Figure 14. The effects of stellar scattering deplete the signal at lower frequencies, however due to the more massive systems in the VDF population, the frequency at which the turn-over happens is lower than for the GSMF population. Even so, the effects of cosmic variance cause the VDF populations at this level of stellar density in galactic cores to never actually reach the expected power-law.

VDF populations coupled with this low-frequency turnover means that these populations never reach the expected power law behavior of a stochastic background.

In conclusion, the VDF populations consist of fewer total sources contributing a large amount to the stochastic background than the GSMF populations. The systems that significantly contribute to the background the most are very massive. Since these massive systems are so few in number, they are more susceptible to the effects of cosmic variance. The implications for detection of spectra like those created by the VDF population has yet to be studied. The peak sensitivity of a PTA is right around $f_{\text{GW}} = 1/T_{\text{obs}}$, so the potential for larger sources at lower frequencies increases the chance of the detection of a single resolvable source. More on detecting individual sources will be discussed in Chapter 5.

3.3 Spectral Shape from Binary Black Hole Dynamics

Distributions of A_{yr} are a useful way of comparing predictions for the stochastic background, and if one assumes gravitational radiation is the dominant evolutionary mechanism for all binaries in the PTA band and that binaries enter the PTA band in circular orbits, then A_{yr} provides all that is needed to describe the expected power-law spectral model from Eqn. 2.6.6. However, those assumptions do not necessarily hold. Instead, it is very likely that as binaries enter the PTA band, they are evolving through some other mechanism (e.g., slingshot interactions with a core of unbound stars) and are not circular. In these cases, the spectral shape deviates from the power-law model, and the specific shape of the spectra will depend on the specifics of the other mechanism driving evolution, as seen above in Figure 15.

While it is fairly straight forward to model circular binary evolution with many mechanisms, once any level of eccentricity is incorporated, the modeling becomes difficult as there are no analytic spectral models that encapsulate the combined influences. Modeling the combined effects requires evolving each binary across the entire PTA band individually since a binary's total mass, mass ratio, and the initial parameters of the evolutionary mechanisms all impact the evolution track. This level of individual detail makes a single spectra calculation take much longer than in the non-circular case. In order to speed up the creation of non-circular binary populations, I interpolate a binary's evolution over the expected range of total mass, mass ratio. The specifics of which are described below followed by an example of the resulting spectra from these eccentric populations.

3.3.1 Stellar Scattering & Eccentricity Evolution

When a binary is evolving through interactions with an isotropic distribution of unbound stars in the galaxy core, the orbital decay is set in part by the dimensionless hardening rate H , while the eccentricity evolution is set in part by the dimensionless eccentricity growth rate K , both described in Sec. 2.4.1. Quinlan (1996) measured H and K through simple scattering experiments, there were improved by Sesana et al. (2006), which reproduced

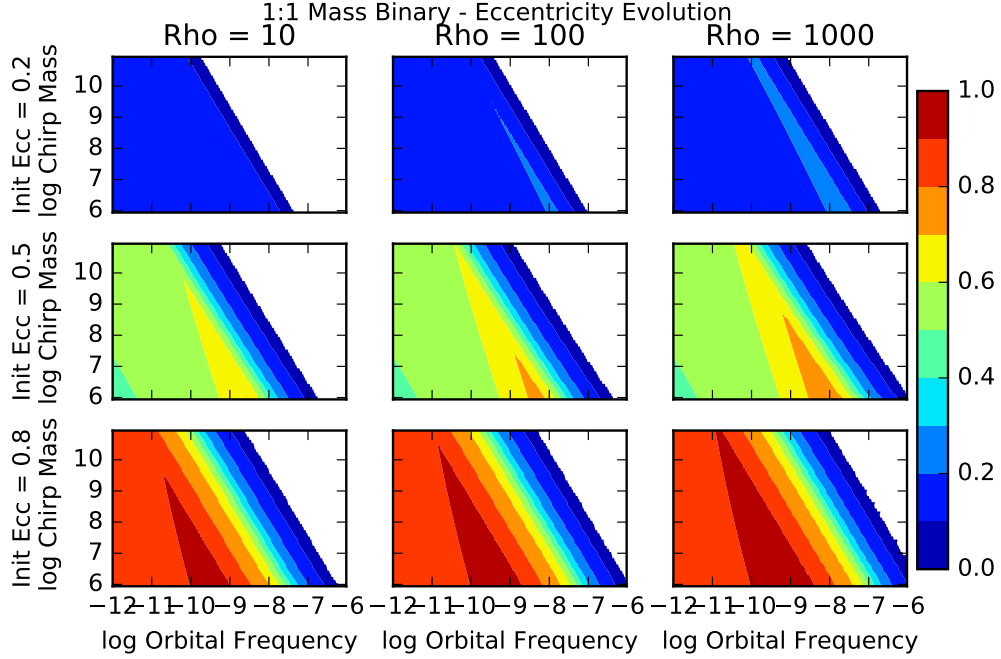


FIGURE 16: The above plot shows the eccentricity evolution of a binary SMBH under a variety of cases. The colors match the binary eccentricity and their values are described in the color bar on the right. The evolution shown here is for equal mass binaries and each individual plot shows the binary chirp mass on the y-axis and the orbital frequency on the x-axis. The columns correspond to increasing levels of stellar density (ρ) and the rows correspond to increasing levels of initial eccentricity (e_0). In general, if the eccentricity starts out small ($e \lesssim 0.3$) then it stays small. However, for higher levels of initial eccentricity, the eccentricity grows as the binary evolves through stellar slingshots. Once the binary evolution becomes dominated by gravitational radiation, the eccentricity quickly goes to zero. The increasing values of ρ move the frequency at which gravitational radiation dominates to higher values, and for the largest values of ρ the frequency where the evolution mechanism changes is within the PTA band. However, even for small values of ρ , if the initial eccentricity is moderately large, the effects of the stellar evolution can be detected in the PTA band by the non-zero levels of eccentricity.

the classical results and found that the rates are well described by the following functions:

$$H = A \left(1 + \frac{a}{a_0} \right)^\gamma, \quad (3.3.1)$$

$$K = A \left(1 + \frac{a}{a_0} \right)^\gamma + B. \quad (3.3.2)$$

Sesana et al. (2006) expanded upon the classical results in Quinlan (1996) to a broader range of initial eccentricities (e_0) and mass ratios (q).

When stellar scattering and eccentricity are incorporated into these models, we interpolate over the results presented in Sesana et al. (2006). Table 1 in Sesana et al. (2006) only shows the values for circular binaries, so unlike Ravi et al. (2014) which ignored the effects of eccentricity on semi-major axis evolution, we use Figure 1 in Sesana et al. (2006) to estimate those effects and include those various values into our interpolation. As in Ravi et al. (2014), we anchor all binary evolution to a starting frequency of $f_{\text{orb}} = 10^{-12}$ Hz, which is sufficiently low that any GW emission is outside PTA sensitivity ranges. The initial eccentricity parameter is set at this frequency, and is evolved across the PTA band in accordance with which ever mechanism (stars or gravitational radiation) dominated the orbital evolution. Figure 16 shows the interpolation of eccentricity evolution across orbital frequency and binary chirp mass under different sets of parameters (ρ , e_0) using the Sesana et al. (2006) scattering experiment results.

3.3.2 Predictions for Full Spectra

The orbital eccentricity and environmental couplings of a population of SMBHBs do not directly impact the merger-rate density. They effect the evolution of the binaries and the frequency distribution of the characteristic strain emitted by each source, $h_c(f_{gw})$. Thus, all populations share a common binary merger-rate density prescription like that described in Section 2.2. However, to ease computational burden, a single measurement of each observable was used: GSMF from Ilbert et al. (2013), f_{pair} from Robotham et al. (2014), and M_\bullet - M_{bulge} from McConnell & Ma (2013). For each realization, the value of each observable was randomly drawn from a Gaussian with widths equal to the cited one-sigma uncertainty regions, this method propagates observational uncertainties through to the spectra variance.

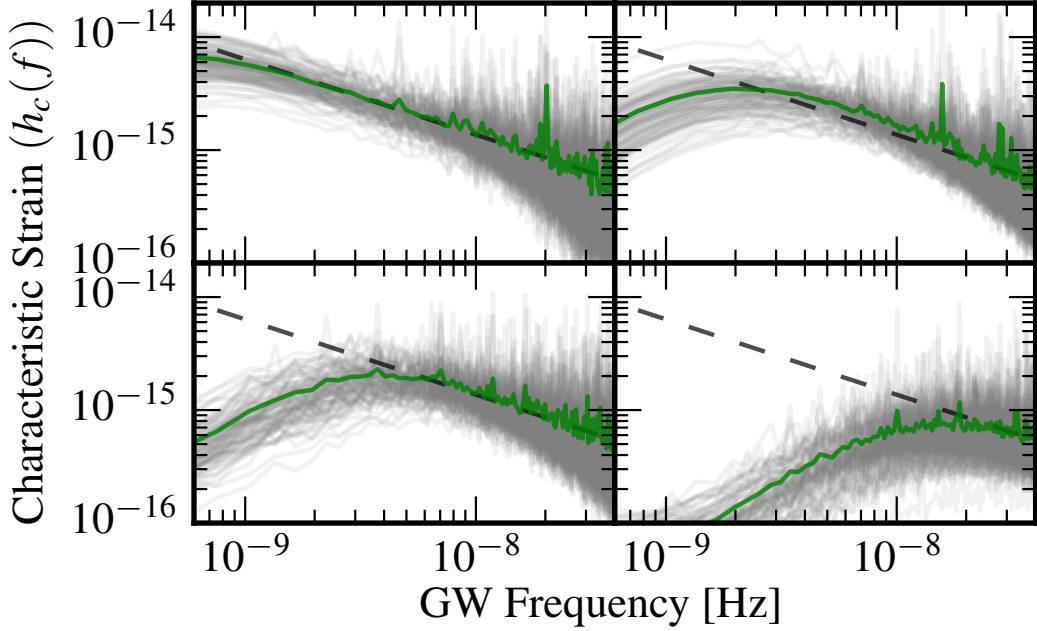


FIGURE 17: The four plots each show a hundred population realizations for the chosen values of binary evolution (e_0, ρ) , where e_0 is the initial eccentricity of the binary set to an orbital frequency of 10^{-12} Hz and ρ is the density of unbound stars in the galactic core. Grey lines indicate single population realizations, while green is the mean over realizations. The dashed line shows a $\propto f^{-2/3}$ strain spectrum for reference. The four plots encapsulate the four extreme corners of the combined parameter space $\{e_0, \rho\}$: upper left $\{e_0 = 0, \rho = 10 M_\odot \text{pc}^{-3}\}$; upper right $\{e_0 = 0.9, \rho = 10 M_\odot \text{pc}^{-3}\}$; lower left $\{e_0 = 0, \rho = 10^4 M_\odot \text{pc}^{-3}\}$; lower right $\{e_0 = 0.9, \rho = 10^4 M_\odot \text{pc}^{-3}\}$.

To generate a population, a finite number of sources are created, whose binary parameters match the merger-rate density for each realization, with eccentricities that have been evolved according to the prescribed environmental conditions $\{e_0, \rho\}$. We assume that all binaries have the same initial eccentricity and are embedded in a stellar distribution with the same density.

Almost all ($> 99\%$) of the GW strain in the PTA sensitivity band ($10^{-10} < f_{gw} < 10^{-7}$ Hz) comes from less than 2×10^5 sources. These sources are saved for each realization. The characteristic strain spectrum of the GW background, $h_c(f)$, is built up as the quadrature sum of the strain from each source. Figure 17 shows the characteristic strain spectra at four extreme corners of the combined parameter space $\{e_0, \rho\}$.

Chapter 4

Astrophysical Interpretation of Pulsar Timing Array Limits

The previous chapter in this dissertation have focused on predicting the gravitational wave signatures from a population of binary SMBHs. While these predictions are interesting and useful in their own right, one of the primary purposes for creating a simulation to produce them was to better understand and interpret PTA data. The following chapter sets out to systematically do that. First, in Section 4.1, by setting up direct mappings between PTA limits on the gravitational wave background (GWB) and the astrophysical parameters that are used as inputs for A_{yr} predictions. And then by taking actual PTA data and setting limits directly on various parameters of galaxy evolution. Section 4.2 does this for parameters that greatly impact A_{yr} predictions, while Section 4.3 sets limits on a combined parameter space that describes binary evolution parameters that affect the spectral shape of the background in the PTA band.

4.1 Translating GWB Limits and Astrophysical Parameters

One of the overarching goals in this work is to provide a mapping of GWB limit/measurement values to specific parameters of galaxy formation. Below, we look at how areas of parameter space correspond to specific values of A_{yr} with an associated error range. In our discussions below we aim to make the following two statements attainable:

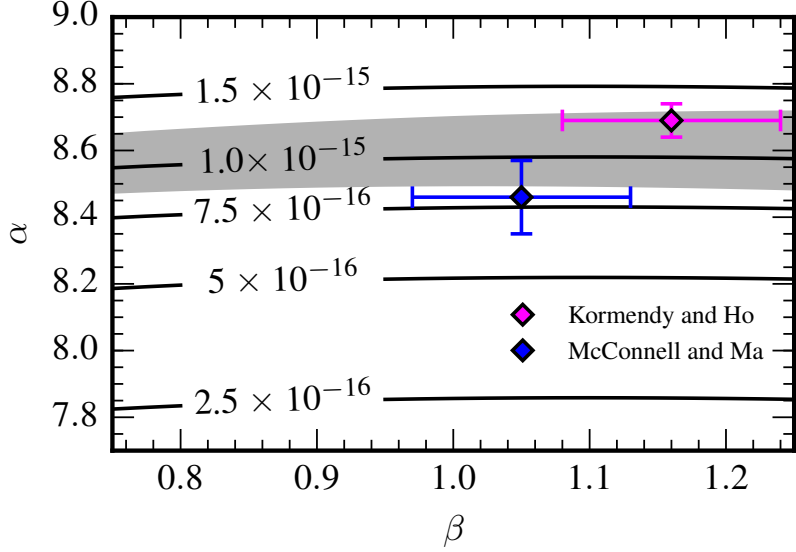


FIGURE 18: These parameters, with ϵ , are used to characterize the black hole-host galaxy relation described in Eqn. 2.3.3 ($\epsilon = 0$ in this figure). The contours show constant values of A_{yr} ; note, however, that the contours will scale downward with $\epsilon > 0$ according to the curve in Fig. 19. Observational measurements are indicated by diamonds. The grey region accounts for uncertainties in other measured astrophysical parameters, specifically the GSMF and the galaxy merger rate. This uncertainty applies to all values of A_{yr} but is only shown on the current best published PTA limit. A set value of A_{yr} translates to a collection of $\alpha - \beta$ pairs, while a PTA upper limit on the value of A_{yr} translates to an upper limit on these parameters. Values of α and β which predict a larger A_{yr} would be inconsistent with that PTA limit.

- Given a PTA upper limit on the GWB, what specifically does this mean for galaxy/SMBH evolution?
- Given a new observation of the M_{\bullet} - M_{bulge} relation, are the new values compatible with the best PTA limit? If not, how can they be reconciled?

4.1.1 GW limits and the Black Hole - Host Galaxy Relation

The parameter space that characterizes the black hole-host galaxy relation is encompassed by α , β , and ϵ (e.g., Equations 2.3.3 & 2.3.5). Fig. 18 shows contours of constant A_{yr} in α - β space, while keeping ϵ equal to zero, as this is the most common way that the M_{\bullet} - M_{bulge} relation is reported. Yet, for a specific value of α , changing β across the entire range of observed values translates to only a $< 20\%$ change in A_{yr} . ϵ is the natural scatter

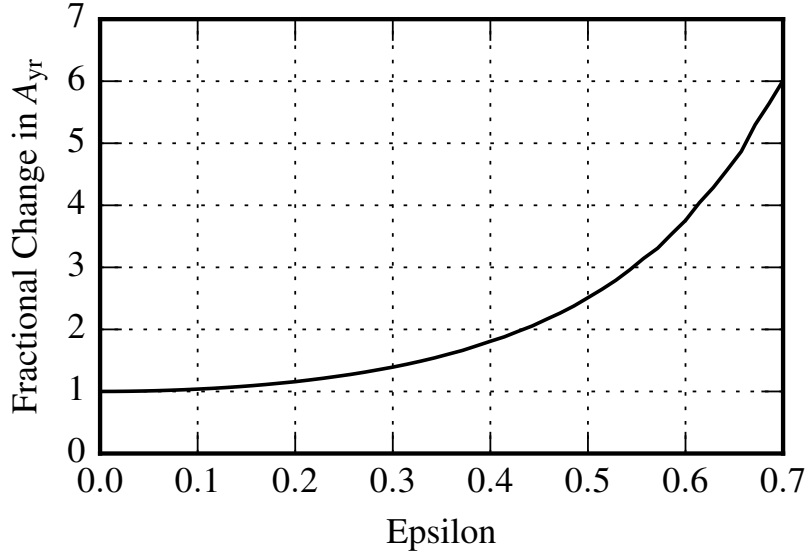


FIGURE 19: As the intrinsic scatter ϵ increases, the black hole mass function adjusts to include higher mass SMBH systems and as such the overall strain increases in an exponential manner.

of individual galaxies around the trend described by intercept α and slope β , and plays a critical role in A_{yr} predictions. As ϵ increases, higher masses are present in a few binaries, which increases the distribution of chirp masses and effectively weights A_{yr} upward. We demonstrate the implications of this in Figure 19, which shows the dependence calculated numerically; for any combination of α and β , changes in ϵ effect A_{yr}^2 in the same way. It is thus α and ϵ that have the most impact on a prediction of A_{yr} , and so we combine the results of Fig. 18 & 19 in Fig. 23 to show A_{yr} as a function of α and ϵ , while holding $\beta = 1$.

4.1.2 GW limits and Stalling Binaries

The assumption that galaxy mergers and binary black holes form at the same cosmological time has until now been implicit in the model used in this paper and others. Yet, as PTA upper limits become inconsistent with measured astronomical parameters, the assumptions of this model must be questioned. It is straight forward to ease this assumption by allowing for a “stall” in the binary SMBH formation, as described in Section 2.4.3. Let us incorporate the variable T_{stall} , which sets the different redshift values used in Equation 2.4.17. Fig. 21 shows how A_{yr} changes with different values of T_{stall} . Obviously

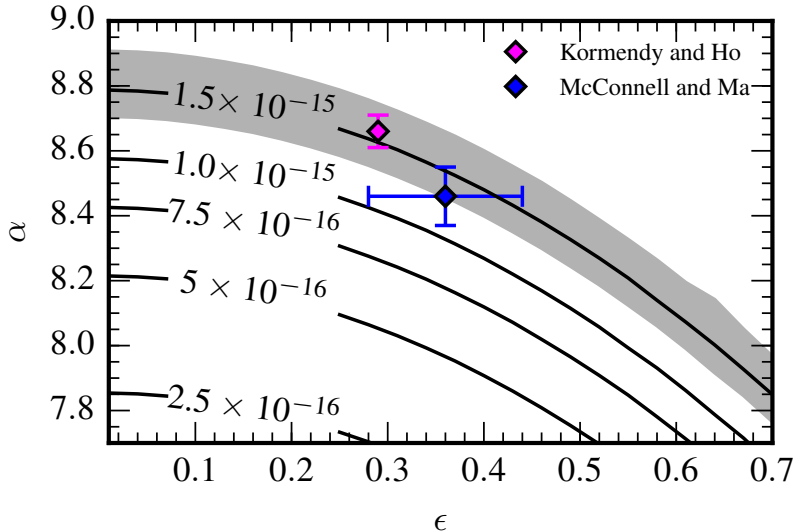


FIGURE 20: The parameters α and ϵ are found to most strongly define the predicted strength of GW amplitude. The contours show the value of the A_{yr} as a function of these parameters. Observational measurements are shown as indicated. The grey region accounts for uncertainties in other measured astrophysical parameters, specifically the GSMF and the galaxy merger rate. As in Fig. 18, this uncertainty applies to all values of A_{yr} but is only shown on the current best published PTA limit. A PTA upper limit on the value of A_{yr} translates to an upper limit on the parameters α and ϵ and would be inconsistent with parameter values that predict a larger A_{yr} .

as the stalling time scale reaches values nearing the Hubble time, A_{yr} falls to zero as no systems are expected to ever enter the PTA band. The meaning and use of limits on T_{stall} are described further in Section 4.2.2.

4.2 Limiting M_{\bullet} - M_{bulge} and stalling timescale with PTA constraints

The following section describes a method by which PTA constraints can be extended beyond A_{yr} and into the parameter space of galaxy evolution. Similar goals have been proposed using different methods in Middleton et al. (2016). We note that a key difference between this work and that of Middleton et al. (2016) is that we interpret PTA limits in the context of other observational constraints on galaxy evolution, whereas the Middleton et al. (2016) method assumes no outside knowledge of the SMBH binary population,

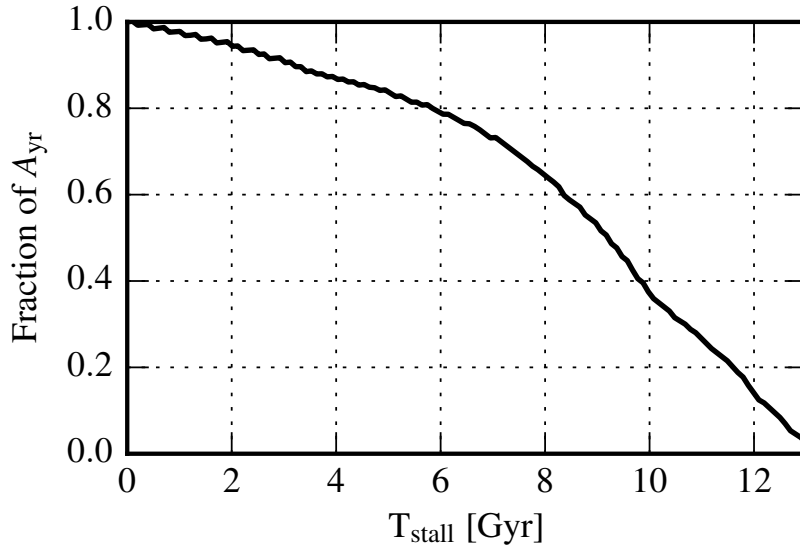


FIGURE 21: T_{stall} measures the time between the galaxy merger and the binary SMBH entering the PTA band in Gyrs, described in Section 2.4.3. The predicted value of characteristic strain for a given value of astronomical parameters depends on the value of T_{stall} . As the time increases, binaries “stall” for longer and less reach the PTA band, which lowers the overall strain until the time approaches a Hubble time and there is effectively no GWB from binary SMBHs.

except for a general form of the SMBH merger rate density (which is well motivated), to formulate their constraints. As such, they were unable to place meaningful limits on the binary population, while this work is able to place tighter constraints by utilizing a well established range of prior information.

4.2.1 Constraining α , β , and ϵ for the M_{\bullet} - M_{bulge} relation with PTAs

It is common for PTA constraints to be quoted as a single number, A_{yr} , which represents the 95% upper limit on a GWB of a given spectral index: for binary SMBHs, $\alpha_{\text{h}} = -2/3$ (Equation 2.6.6). However, quoting a single number is only for simplicity; the actual result produced by PTAs for a limit on a power-law GWB is a probability distribution for the value of the strain amplitude.

Here we describe the use of this probability distribution to obtain direct limits on α , β , and ϵ . We then demonstrate how an inconsistency with an observed value can be used to place a lower limit on T_{stall} .

In terms of Bayesian statistics, a PTA produces a posterior on A_{yr} ,

$$p(A_{\text{yr}}|\text{PTA}) \propto p(A_{\text{yr}}) p(\text{PTA}|A_{\text{yr}}), \quad (4.2.1)$$

where $p(A_{\text{yr}})$ is the prior distribution, and $p(\text{PTA}|A_{\text{yr}})$ is the likelihood. We are interested in producing a posterior on parameters from our model. As the M_{\bullet} - M_{bulge} relation provides the most influential parameters on A_{yr} , here we calculate the posteriors on α , β , and ϵ :

$$p(\alpha, \beta, \epsilon|\text{PTA}) \propto p(\alpha) p(\beta) p(\epsilon) p(\text{PTA}|\alpha, \beta, \epsilon). \quad (4.2.2)$$

Our model gives us a way of translating α , β , and ϵ into a value of A_{yr} , which means the two likelihoods are equivalent,

$$p(\text{PTA}|\alpha, \beta, \epsilon) = p(\text{PTA}|A_{\text{yr}}(\alpha, \beta, \epsilon)). \quad (4.2.3)$$

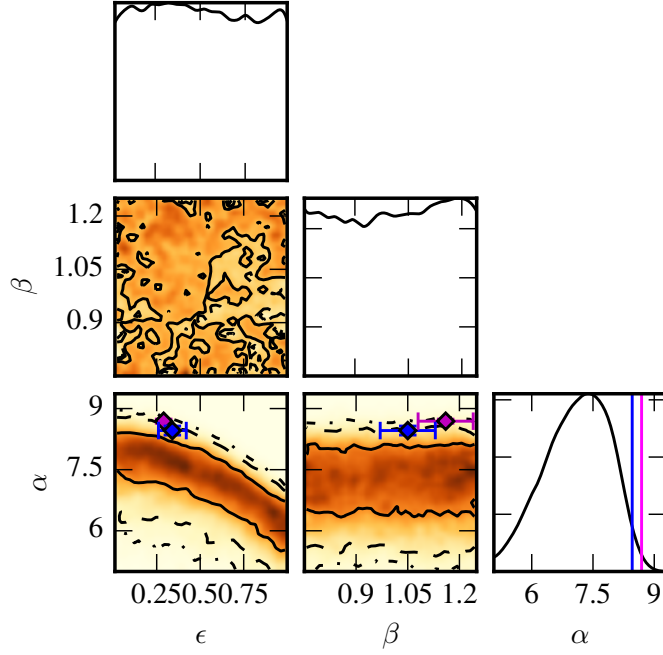
We do need to include other observational parameters into our model, specifically the GSMF and the galaxy merger rate. We will represent all of these parameters with θ , which we can marginalize over, giving

$$p(\alpha, \beta, \epsilon|\text{PTA}) \propto \int d\theta p(\theta) p(A_{\text{yr}}(\alpha, \beta, \epsilon, \theta)|\text{PTA}). \quad (4.2.4)$$

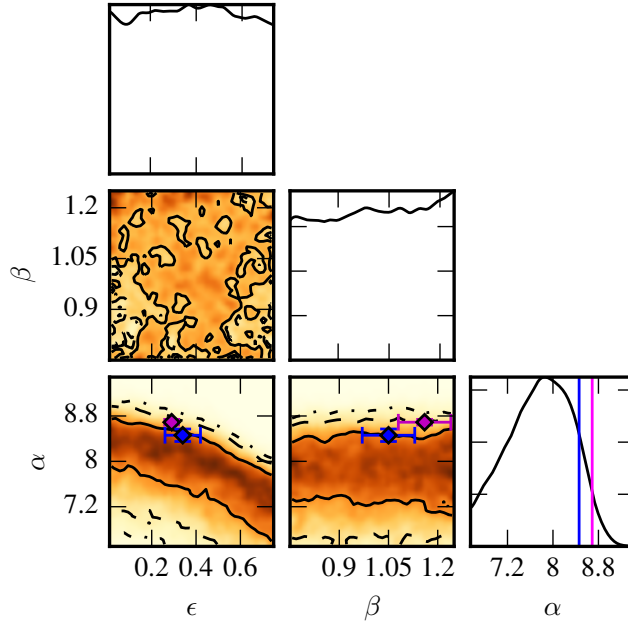
Fig. 22a shows the translation of the recent upper limit from Shannon et al. (2015) into the parameter space that characterizes the M_{\bullet} - M_{bulge} relation, while Figure 22b shows the translation of the recent upper limit from Arzoumanian et al. (2015) into the same parameter space. A 95% upper limit can be set in the $2 - D$ parameter space, α - ϵ , by integrating the distribution. These are shown in Figures 23a & 23b for the Shannon et al. (2015) and the Arzoumanian et al. (2015) upper limits, respectively. Similar work has been done in Middleton et al. (2016), where an attempt is made to reconstruct a parametrized form of the black hole merger rate density from a posterior on A_{yr} from PTAs. This kind of mapping from PTA data to astrophysical parameters is the next step forward in analyzing PTA data and is already being used in recent PTA limit papers (Arzoumanian et al. 2015).

4.2.2 Reconciling PTA limits with M_{\bullet} - M_{bulge} measurements

Figure 23 demonstrates that the Kormendy & Ho (2013) and McConnell & Ma (2013) measurements are inconsistent with the upper limit on the GWB from Shannon et al.

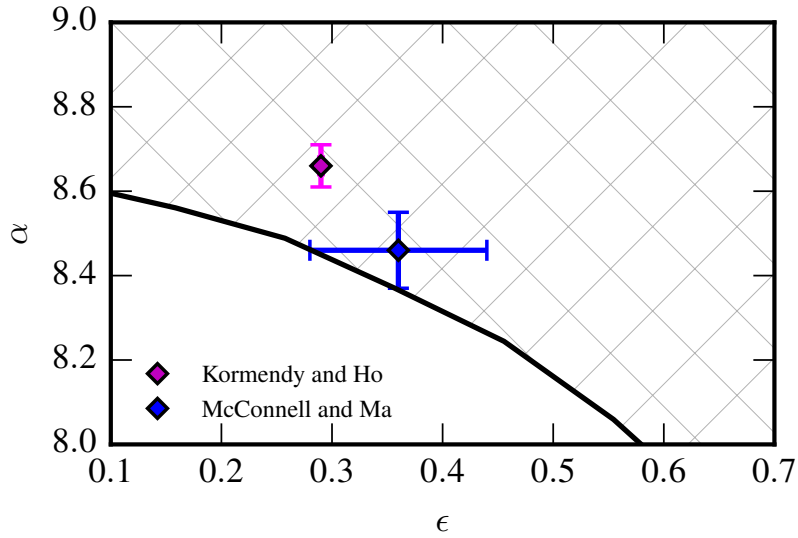


(A) PPTA 11 year

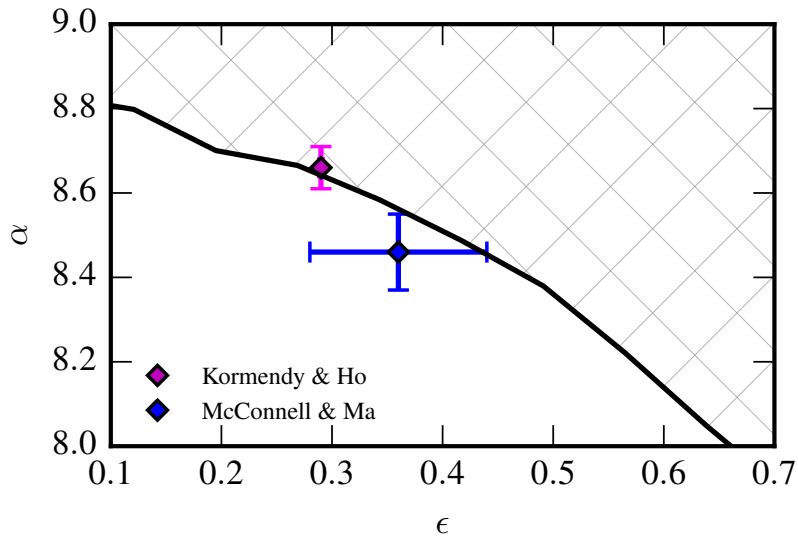


(B) NANOGrav 9 year

FIGURE 22: The above plots show the translation of the marginalized posterior distributions of A_{yr} from (a) Shannon et al. (2015) and (b) Arzoumanian et al. (2015) into the black hole - host galaxy parameter space, which is characterized by an intercept α , a slope β , and an intrinsic scatter ϵ . β is not informed by the distribution of A_{yr} , while both α and ϵ are, with a limit on α being more strongly set. The curves show the 1, 2, and 3σ contours. Relevant observational measurements are also shown, with McConnell & Ma (2013) in blue and Kormendy & Ho (2013) in magenta.

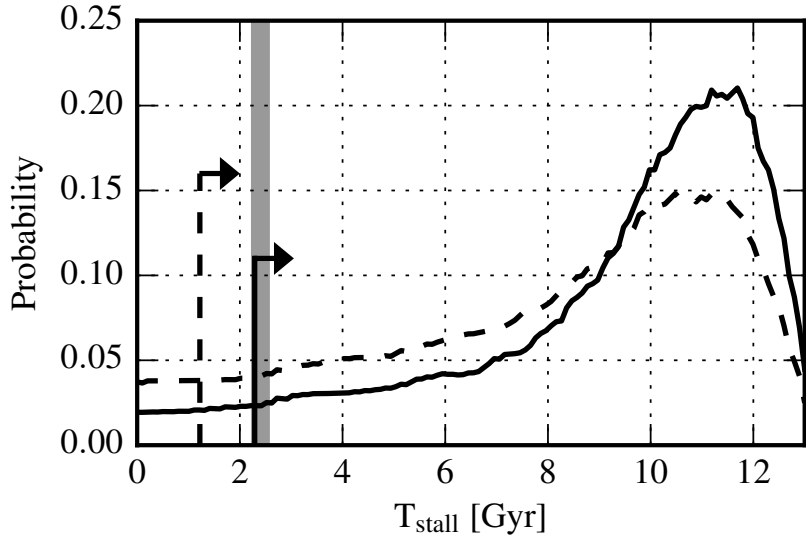


(A) PPTA 11 year

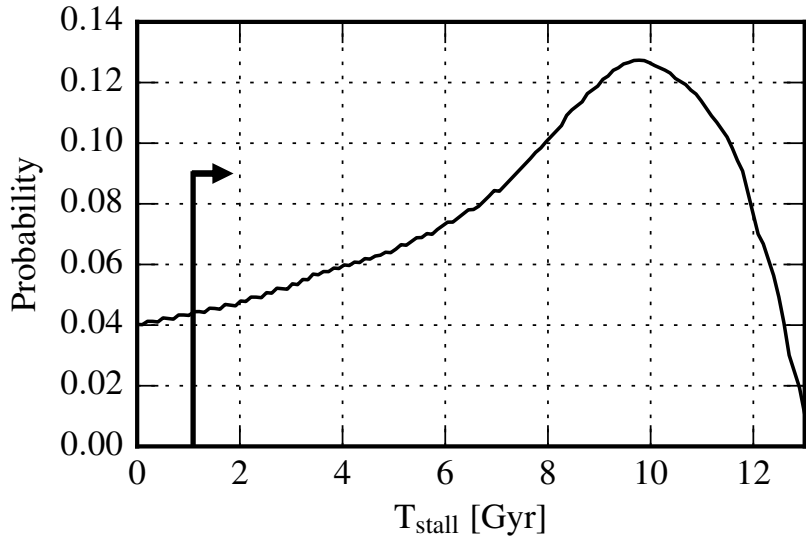


(B) NANOGrav 9 year

FIGURE 23: These plots show both the PPTA 11 year limit (Shannon et al. 2015) and the NANOGrav 9 year limit (Arzoumanian et al. 2015) on A_{yr} translated directly into the parameter space of α - ϵ , which characterizes the black hole - host galaxy relation. The solid line in each represents the 95% upper limit on this combined parameter space. The points above the line are inconsistent with a power-law spectra associated with the predicted A_{yr} values for the fiducial model, discussed in Section 3.1.4. Observed values of these parameters are shown with errorbars, McConnell & Ma (2013) in blue and Kormendy & Ho (2013) in magenta.



(A) PPTA 11 year



(B) NANOGrav 9 year

FIGURE 24: Using the measured parameters of the M_{\bullet} - M_{bulge} relation from Kormendy & Ho (2013) and McConnell & Ma (2013) the above plots show a probability distribution of T_{stall} , the time between the galaxy merger and the binary SMBH entering the PTA band in Gyrs. (a) Uses the posterior distribution on A_{yr} from Shannon et al. (2015), and sets a lower limit of 1.2 and 2.3 Gyrs for the α, ϵ values of McConnell & Ma (2013) and Kormendy & Ho (2013), respectively. The shaded gray region is upper limit on the amount of T_{stall} expected from the simulations in Khan et al. (2013). (b) Uses the posterior distribution on A_{yr} from Arzoumanian et al. (2015), and sets a lower limit of 1.1 Gyrs for the α, ϵ values of Kormendy & Ho (2013).

(2015), while Kormendy & Ho (2013) is inconsistent with the upper limit from Arzoumanian et al. (2015). We can thus attempt to reconcile this discrepancy by considering whether a non-zero T_{stall} can make these two results consistent. If we assume the measured values are correct, then we can do a direct translation of the PPTA upper limit into a probability distribution on T_{stall} . This is seen in Fig. 24a, and we set a lower limit of $T_{\text{stall}} > 2.3$ Gyrs using Kormendy & Ho (2013) and a lower limit of $T_{\text{stall}} > 1.2$ Gyrs using McConnell & Ma (2013). We do the same thing for Kormendy & Ho (2013) and the NANOGrav upper limit, seen in Figure 24b, and we set a lower limit of $T_{\text{stall}} > 1.1$ Gyrs.

We reiterate that in our formulation, τ essentially represents a dynamical friction timescale (the merger timescale), while T_{stall} represents the additional time it takes the binary to enter the PTA waveband. Our limits on T_{stall} could be capturing a longer merger timescale, such as those discussed in Ravi et al. (2015). However, since there is not a concrete definition for each of these parameters in the literature, we choose to make the straight-forward assumption that after a standard dynamical friction timescale estimate, the remaining time for binary evolution is captured by T_{stall} .

There are a limited number of observational and theoretical limits on stalling timescales in the literature. Originally, the apparently “missing” inspiral mechanisms were taken to imply that binary SMBHs might stall for up to a Hubble time (Begelman et al. 1980), although for a few systems with sufficient gas it was shown that binary SMBHs can inspiral efficiently (e. g. Mayer et al. 2007; Cuadra et al. 2009). More recently, numerical simulations have demonstrated that with mild triaxiality or axisymmetries in merging galaxies, binary SMBH coalescence timescales can be pushed to $\lesssim 2.4$ Gyr, and contrary to previous inference, timescales have been found to be much less (< 0.5 Gyr) for the highest-mass galaxies (Preto et al. 2011; Khan et al. 2011, 2013). Furthermore, Burke-Spolaor (2011) placed an observational upper limit on the stalling timescale of the most massive binary SMBH systems ($\gtrsim 10^8 M_{\odot}$) of < 1.25 Gyr at 50% confidence (i. e. a few Gyrs at 95% confidence). The latter observationally-derived value is consistent with our lower limits using both the McConnell & Ma (2013) and the Kormendy & Ho (2013) relations. However, the theoretical result that inspiral due to host axisymmetries can be

$\lesssim 2.4$ Gyr, or beyond < 0.5 Gyr for the highest-mass galaxies we’re probing here, is in contention with both of these limits. More recent work has shown that for ‘dry’ mergers, where there is little gas present, the total merger time is > 1 Gyr, which is consistent with our limits (Sesana & Khan 2015).

There are two likely interpretations of this result. First, if we assume that the M_{bulge} relations here hold, we must infer that either something else is reducing the expected GW background (for instance, a turn-over due to environmental coupling or a longer merger timescale than assumed here), or that triaxiality and axisymmetry are not prevalent enough to be the dominant force in driving pre-GW-dominant inspiral in massive galaxies. Second, it is possible that the parameterizations of M_{bulge} relations have been over-estimated. As a more general consideration for this analysis, it is worth noting here that it has been suggested that recent black hole - host relations might err on using an upper-limit mass value for many black holes in their fits, for a range of valid values Merritt (2013, see e. g. the discussion in Chapter 3.). Thus, it is possible that the McConnell & Ma (2013) and Kormendy & Ho (2013) measurements have arrived at disproportionately high values, particularly for α and ϵ . Recent work has proposed there is a bias in these measurements as well (Shankar et al. 2016), we note that a moderate downward shift of both the McConnell & Ma (2013) and Kormendy & Ho (2013) relations in α and/or ϵ would render fits consistent with current PTA limits (e. g. Figure 23).

As previously noted, there could exist a deviation from a single-power-law GWB spectrum due to essentially the opposite effect from stalling: a super-efficient evolution through low orbital frequencies that also affects the PTA band. This may lead to a low-frequency turn-over in the strain spectrum and significant additional complexity to PTA analysis (e. g. Ravi et al. 2014; Huerta et al. 2015; Sampson et al. 2015; Arzoumanian et al. 2015). The next section investigates that possibility.

4.3 Limiting the multidimensional parameter space of binary evolution using Gaussian Process Regression

For non-circular binaries, there does not exist an analytic spectral model, and so a direct sampling of parameter space, which would require the creation of a unique spectra, is prohibitively long and prevents analysis like the kind presented above in Section 4.2. To bypass this issue, we use gaussian process regression, which is a powerful interpolation scheme which treats (noisy) data as a random draw from a multivariate Gaussian process with a mean vector and covariance function. A set of initial training data is used to learn the GP’s covariance structure, after which predictions can be made about the outcome of hypothetical experiments between the training points (interpolation), and beyond them (extrapolation). We use the set of spectra from the populations described in Section 3.3 as training data and then analyze a dataset that is identical to that from Arzoumanian et al. (2015) to set limits on the combined parameter space of $\{e_0, \rho\}$, where e_0 is the initial eccentricity of the binary set to an orbital frequency of 10^{-12} Hz and ρ is the density of unbound stars in the galactic core. Both are key parameters for binary evolution (Section 2.4).

The procedure is as follows:

1. **Simulate training data:** Build a bank of SMBHB populations by initializing simulations with different binary eccentricities and environments.

[Computationally expensive].

2. **Train the Gaussian-process model:** Model the strain distribution over population realizations as Gaussian with a mean and standard error. This noisy data is used to train a GP and optimize its kernel hyper-parameters.

[Computationally cheap].

3. **Analyze PTA data with Gaussian-process model:** The trained GP predicts the shape of the strain spectrum for our GW analysis.

[Computationally cheap].

The dataset used to perform the analysis consisted of an 18-pulsar array that emulates the Arzoumanian et al. (2015) PTA in every way, with the same noise properties and an

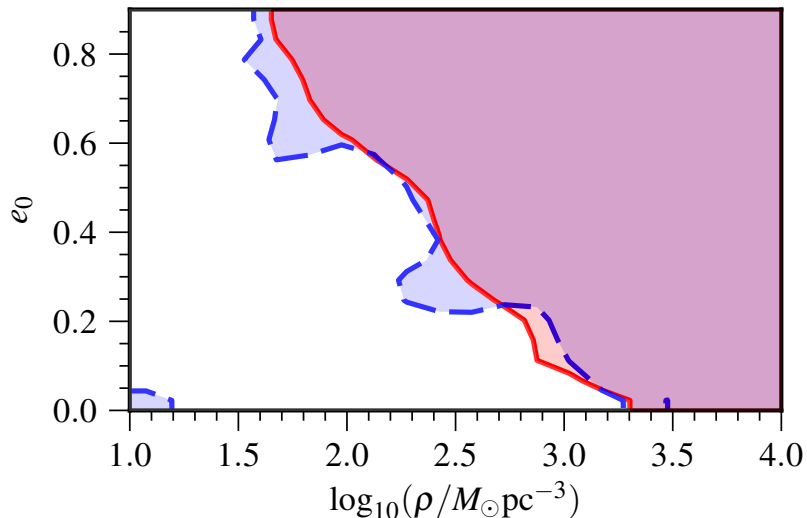


FIGURE 25: Astrophysical inference on an emulated NANOGrav 9 year dataset. The GSB amplitude at high frequencies is anchored to the McConnell & Ma (2013) (blue) and the Kormendy & Ho (2013) (red) A_{yr} distributions plotted in Figure 6. The lines indicate the boundaries of the 68% credible regions.

identical observation schedule. The amplitude is anchored for the two A_{yr} predictions plotted in Figure 6, which are made using two different measurements of the M_{\bullet} - M_{bulge} relation. The shape of the spectra is then informed by the training data. The resulting 2-d marginalized posterior distribution in $\{e_0, \rho\}$ are shown in Figure 25. Under the assumptions of the given A_{yr} priors, the emulated NANOGrav 9 year data favors eccentric binary SMBHs that are coupled to dense stellar distributions. This is because a power law spectrum produces a signal that is inconsistent with the PTA data, as seen and discussed above in Section 4.2. In this case, instead of using T_{stall} to explain the discrepancies, they can be explained by the existence of a low-frequency attenuation caused by eccentricity and the binary’s interaction with the stars in the galactic core. We note that the McConnell & Ma (2013) prediction on A_{yr} is just within in credible region, so a power law spectra has not been ruled out completely for that model. However, a modest eccentricity with low stellar densities is ruled out because the shape of the spectra under those circumstances actually grows larger than that of a power law spectra at the frequency where the NANOGrav limit is set.

Chapter 5

Electromagnetic Counterparts for Binary Supermassive Black Holes

All of the work described so far in this dissertation has kept electromagnetic and gravitational wave observations separate using one to inform the other, like taking observations of galaxies to infer the binary population, or using PTA limits to constrain black hole - host galaxy or binary dynamical parameters. In this next chapter, the models for gravitational wave sources described so far will be combined with electromagnetic models of active galactic nuclei (AGN) to study the potential for multi-messenger sources present in the PTA band. The first section describes the types of dual AGN that are included in these models, followed by a discussion of the potential for detecting a multi-messenger source with future PTAs.

5.1 Incorporating Models for Dual AGN

The accretion process onto SMBHs, which powers AGN, requires large clouds of gas in the interstellar medium to lose enough angular momentum to plunge close enough to a galaxy's core to be gravitationally captured by the SMBH's accretion disk. Simulations have shown that major merger events are effective mechanisms to drive gas into the common core of the merger remnant (Hopkins et al. 2006). Recent observations have also hinted that galaxy mergers may preferentially trigger high-luminosity AGNs (Comerford & Greene 2014), and radio loud AGNs appear to almost always be associated with a

major merger (Chiaberge et al. 2015). Other evidence indicates that the AGN fraction of major mergers increases as the binary goes to smaller separations (Ellison et al. 2011). All of this points to a strong connection between dual AGN and galaxy mergers.

Given that a lot of AGN activity is triggered by galaxy mergers, there are many signatures for dual AGN across the electromagnetic spectrum (Burke-Spolaor 2013). Modeling these various electromagnetic counterparts has various challenges, and since there has been no combining of electromagnetic models with gravitational wave models, we start by exploring two of the easiest AGN tracers to model: dual radio AGN and peculiar emission lines.

5.1.1 Dual Radio AGN

One of the most straight forward ways to identify two SMBHs in close orbit is by spatially resolving them. Compact self-absorbed synchrotron emission at the site of relativistic jet formation is detectable by radio telescopes. While current searches have only revealed one sub-100 parsec pair, at a projected separation of 7 pc (Rodriguez et al. 2006), in principle, this type of radio emission should be sustainable throughout the evolution of the binary. The VLBA has excellent resolving power down to sub-milliarcseconds. While these kind of sources are not practical to discover in large-scale blind searches (Kaplan et al. 2011), they are ideal tools for targeted candidate confirmation, such as the follow-up to a PTA detection of a resolvable binary in gravitational waves (Croft & Kaplan 2016).

Modeling dual radio AGN requires two additional parameters: angular separation (α) and radio flux (S). Angular separation is calculated, in degrees, by:

$$\alpha = \frac{a}{D}, \quad (5.1.1)$$

where D is the distance to the source, a is the orbital semi-major axis and q_{\bullet} is the black hole mass ratio. The radio flux, S , is drawn from the bivariate luminosity functions from Mauch & Sadler (2007), which relate S to the K -band magnitude of the galaxy. The K -band magnitude is calculated from the stellar mass of the galaxy M_{Gal} using the relation from Cappellari (2013).

$$M_K = \frac{10.58 - \log M_{\text{Gal}}}{0.44} - 23 \quad (5.1.2)$$

5.1.2 Peculiar Emission Lines

For two active black holes in approximately circular orbits, their relative line-of-sight velocity (v_{rel}) can be estimated by

$$v_{\text{rel}} = \sqrt{\frac{GM_{\text{tot}}}{a}} \sin i , \quad (5.1.3)$$

where M_{tot} is the total mass of the binary black hole system, a is the orbital semi-major axis, and i is the inclination angle. If any, or both, of the black holes are AGN with either broad or narrow emission lines, then these emission line regions may become either red- or blue-shifted with respect to the host galaxy or the companion black hole by several hundred km s^{-1} .

This method has been used to successfully identify many dual AGN at early stages of inspiral (Comerford et al. 2013). However, at separations for binaries within the PTA band, nothing to date has been verified as a true binary, as care must be taken to rule out other non-binary emission dynamics which could cause similar features.

5.2 Predictions for ‘Multi-Messenger’ Sources in the PTA Band

When modeling the stochastic background, we work in characteristic strain (h_c), but when discussing individually resolvable sources we work in terms of strain (h_s from Equation 2.5.1). Figure 26 plots the combined brightest sources in the PTA band from a thousand populations which were created using σ as a proxy for the black hole mass, a method derived in Section 3.2. Plotted on top of that distribution are predictions of PTA sensitivity curves for the next decade or so (most PTAs already have over a decade of data) (Ellis 2016). While there has been no detection to date, this is not surprising, but over the course of the next decade PTA sensitivities will reach a region where the probability of detecting a single resolvable source will get very high.

Each of the 1000 populations are then modeled with AGN emission. Figure 27 shows the parameter distributions for the dual radio AGN sources. These sources are very rare, with each realization having about 0.5 dual radio AGN sources in it, but the sources that are present are observable with present radio telescopes, as they have large fluxes and are nearby. Figure 28 shows the parameter distributions for the binaries emitting

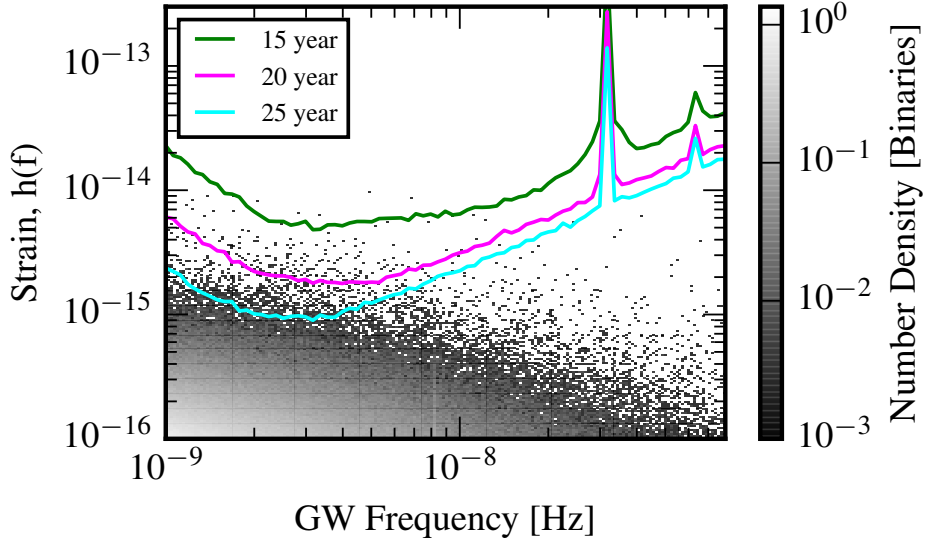


FIGURE 26: All of the points in this plot represent the estimated number density of sources at a given strain and gravitational wave frequency from 1000 different populations of binary SMBHs. The three different colored lines show increasing PTA sensitivity over the next decade. Over the next decade, the improvement of sensitivity should allow for the detection of an individually resolvable source.

GWs in the PTA band which contain potentially resolvable peculiar emission lines. For a peculiar emission line to be resolvable, we claim that the velocity offset must be larger than the velocity dispersion of the host galaxy and smaller than the Roche lobe limit of the individual sources. These are conservative limits, but we use them in an attempt to maximize the likelihood that the offset emission lines would be distinct from the rest of the host galaxy's spectra. These types of sources are much more numerous, however, their numbers depend on the assumed AGN fraction within the PTA band. Assuming a 50% fraction yields 5000 sources with at least a single AGN detectable by peculiar line emission, 250 of which are dual AGNs. When a 10% AGN fraction is used these numbers drop to 1000 sources with at least a single AGN and 50 duals.

We combine the electromagnetically observable sources with the gravitational wave sources in Figure 29. Multi-messenger sources, which would be detectable with both some kind of electromagnetic counterpart, in addition to gravitational waves, are rare. They appear to be more prevalent at lower frequencies, which is encouraging for future detection prospects. There is currently an open question regarding low-frequency attenuation of the

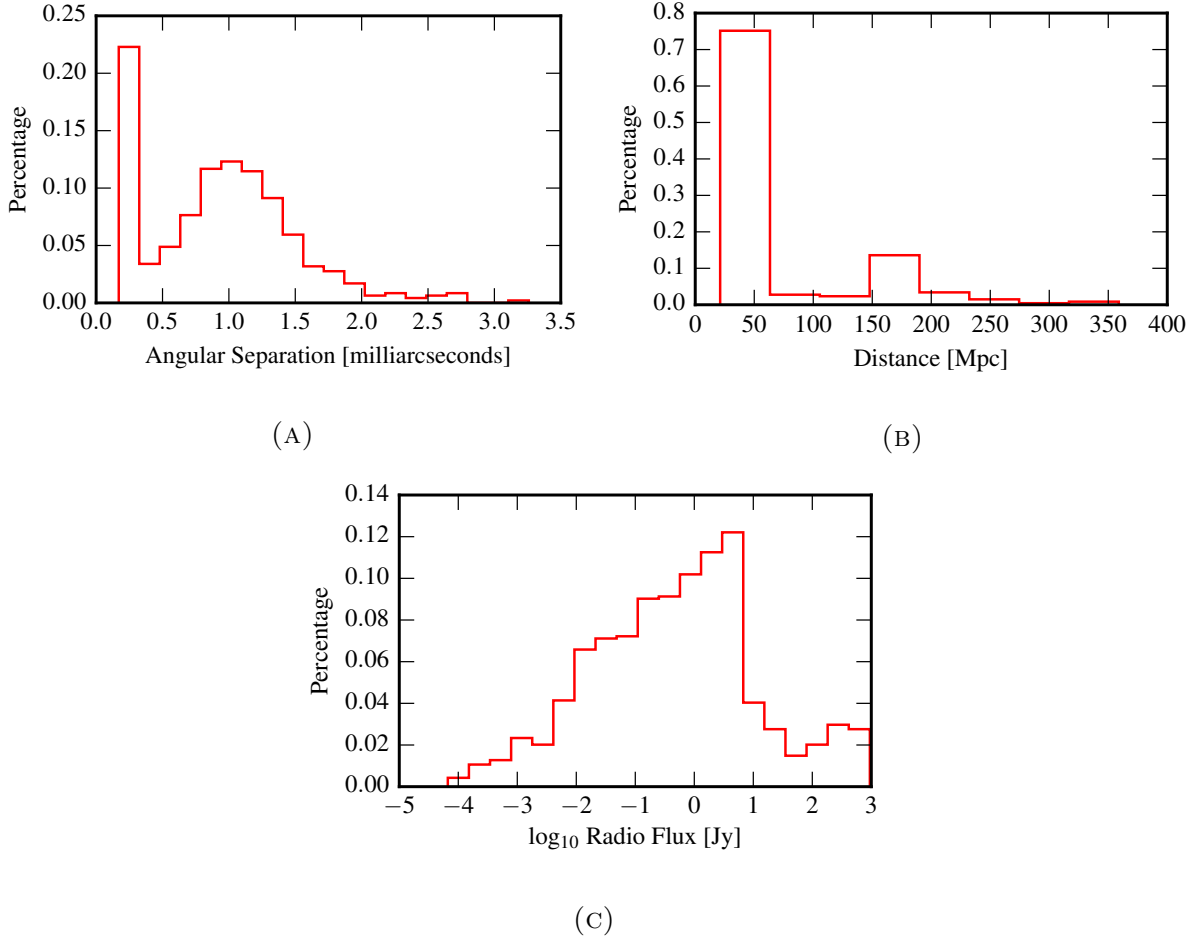


FIGURE 27: The above plots show various parameter distributions for the binaries which contain two radio loud AGN. They are very rare, as there is 0.5 sources per realization. However, the sources that do show up have large fluxes (C), are at very small distances (B), and should be at VLBA resolvable separations (A).

stochastic background due to environmental effects, and so electromagnetic counterparts to binary SMBHS, even non-PTA-resolvable sources, may play a big role in determining the population demographics at the lower end of the PTA frequency band.

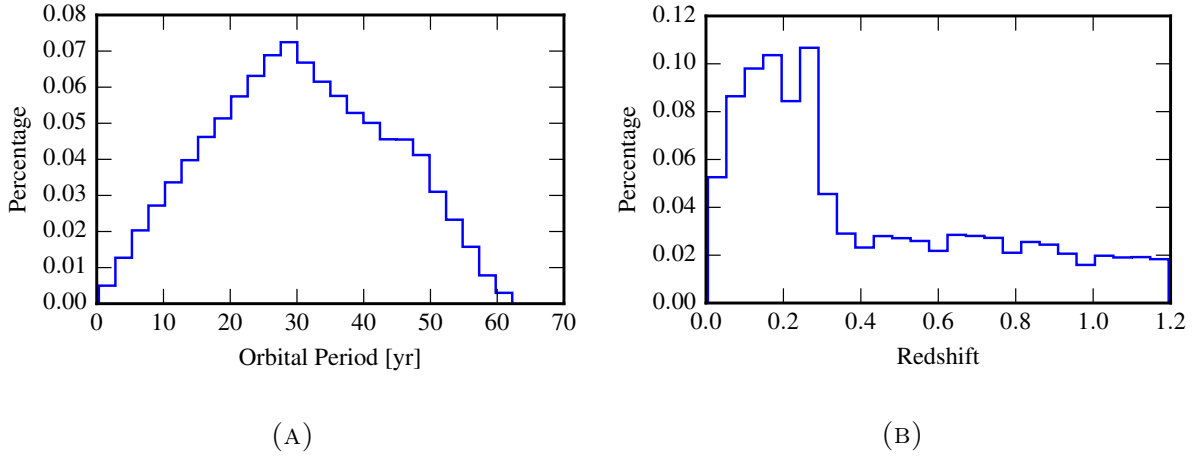


FIGURE 28: The above plots show various parameter distributions for the binaries emitting GWs in the PTA band which contain potentially resolvable peculiar emission lines. Both orbital period (A) and redshift (B) will set the detectability of these sources. The distributions stay fairly constant, but the numbers are based on what the AGN fraction is at binary separations in the PTA band, which are unknown. When we use a 50% AGN fraction we discover around 5000 sources with at least a single AGN with a potentially detectable peculiar emission line, 250 of which are actual dual AGNs. These numbers drop to 1000 sources with at least a single AGN and 50 duals when we drop the AGN fraction to 10%.

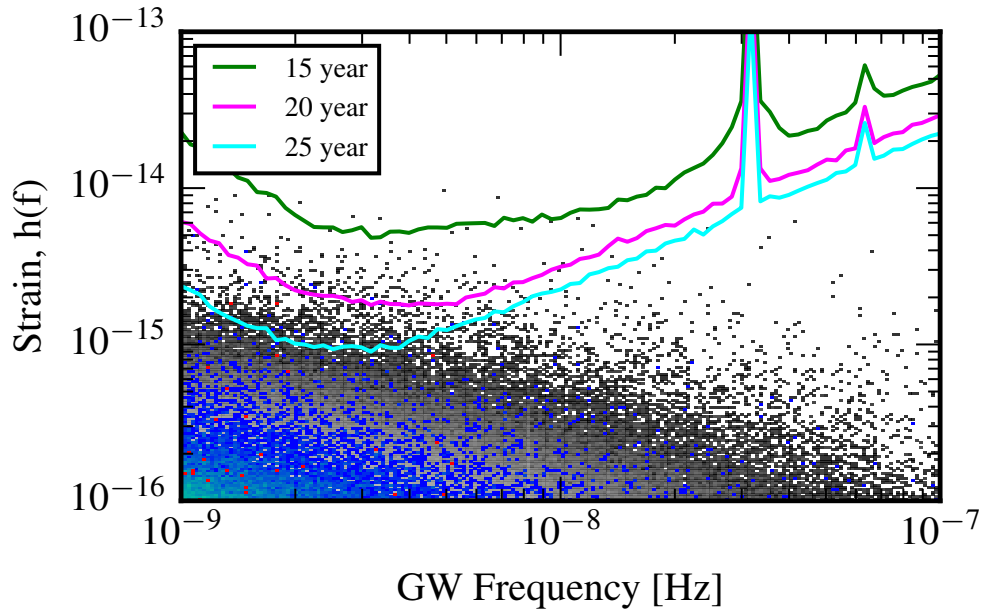


FIGURE 29: This plot overlays the distributions of dual radio AGN sources (red) and peculiar line emission sources (blue) over the gravitational wave sources from Figure 26. While multi-messenger sources appear to be rare, they do appear to occur more prevalently at low frequency, which is encouraging given PTA sensitivity curves.

Chapter 6

Summary

This dissertation has given a detailed description of the models used to create populations of binary SMBHs, which can then be utilized to understand and interpret PTA data in an astrophysical context. Using these models, I have inspected the amplitude variance of the nHz- μ Hz waveband GWB, as formulated from state-of-the-art observations of massive galaxies, massive galaxy mergers, and SMBHs in the $z \lesssim 3$ Universe. In the course of this analysis I provided simple reference plots which can be used to map PTA limits on the GWB to the parameters of cosmological evolution that most impact the power-law GWB prediction (Figs. 19 & 21).

I found that the vastly different observations of the intercept (α) and scatter (ϵ) of the M_{\bullet} - M_{bulge} relation have the most impact on the range of GWB amplitude prediction. I used PTA upper limits on the GWB to compare my mapping to these parameters, and found that under some circumstances the M_{\bullet} - M_{bulge} relations of McConnell & Ma (2013) and Kormendy & Ho (2013) are inconsistent with the PTA limit. Both of these measurements include the high-mass SMBHs expected to contribute the majority of signal to the PTA gravitational wave band (Kormendy & Ho 2013; McConnell & Ma 2013), making them the appropriate measurements for this comparison. I showed that using different proxies for the black hole mass function can produce very different population demographics in the PTA band, and further study is needed to assess the impacts these populations have on detectability.

Observationally, the uncertainty in M_{\bullet} - M_{bulge} and similar relations are largely due to

small sample sizes. One important conclusion drawn from this analysis is that better constraints on the M_{\bullet} - M_{bulge} relation will greatly tighten GWB predictions, motivating further SMBH measurements to be made in the $\gtrsim 10^9 M_{\odot}$ range. Furthermore, it has been pointed out that the masses used for many SMBH - host galaxy relations may be overestimated, potentially solving the discrepancy we have found, as recently noted in Shankar et al. (2016). However, this only points more strongly towards a need for better characterization of these relations to allow an accurate prediction of the GWB, which I intend to pursue in more detail in future work. The host-galaxy relation is the most critical to be improved if we are to tighten the constraints PTAs can put on effects such as binary stalling, wandering SMBHs, and environmental interactions from the influence of gas or stellar dynamics during the GW-dominant regime. Finally, while the redshift evolution of this relation was not considered in this work, it is clear that strong evolution could further heighten its impact on GWB predictions (see, e. g., Ravi et al. 2015).

As discussed in Sections 4.2.2 & 4.3, this inconsistency can be reconciled in a number of ways. First, we can include a moderate amount of “stalling” in the inspiral of the binary SMBH, in which the pair slows its evolution for at least 1.2 and 1.1 or 2.3 Gyr for the α, ϵ values of McConnell & Ma (2013) and Kormendy & Ho (2013), respectively, which are in contention with theoretical work that has shown how axisymmetries may allow inspiral efficiencies of < 0.5 Gyr for the most massive pairs. Additionally, we can allow for binary dynamics with the galactic core environment and non-circular orbits to attenuate the signal at the lowest frequencies in the PTA band. The Gaussian Process regression techniques, which were recently published in Taylor et al. (2017), show lots of promise to expand the astrophysical inference that PTAs can do and are sure to be incorporated in future PTA data analysis.

Finally, I shows some preliminary work that incorporates peculiar AGN emission lines and double radio AGN into gravitational wave models. While the prospects for detecting an individually resolvable source with PTA data is still probably a decade or more away, there is some potential that in the future one of those resolvable sources would contain a detectable electromagnetic counterpart.

6.1 Future Work

6.1.1 Expanding Models for Black Hole Mass

The recent debate in the SMBH community calls current observations of the black hole - host galaxy relationship into question. Shankar et al. (2016) claims there is a ‘bias’ in previously reported observations which is causing an over-estimation of black hole masses in the universe. However, Thomas et al. (2016) shows that the most massive black holes and galaxies are more related by size than mass which implies some black hole masses will be even larger than previously thought. The results presented in Section 3.2, which utilize σ as a proxy for black hole mass appear more in line with the Thomas et al. (2016) observations, while recent PTA limits appear more consistent with the Shankar et al. (2016) results. This debate is ongoing and has important implications for potential PTA discoveries since the more massive black hole binaries radiate stronger GWs, and evolve quicker than their smaller counterparts. The most massive systems dominate the stochastic background, and the most massive binaries at the smallest distances are the most likely sources to be detected individually as discrete sources of GWs by PTAs.

6.1.2 Incorporating Electromagnetic Observations

The preliminary work described in Chapter 5 needs to be expanded to include high-energy counterparts (Roedig et al. 2014), complex AGN variability (Smailagić & Bon 2015), and post-merger remnants such as afterglows (Tanaka et al. 2010) and recoiling AGN. Like dual radio AGN, resolving dual x-ray cores is not practical for large-scale blind searches with current x-ray and radio instruments given the small sizes of these objects. However, such emission is an excellent tool for targeted confirmation of candidate binary systems.

For systems with relatively short orbital periods, $P \lesssim 10$ yr, periodic or nearly periodic variability on a time scale associated with the period of the binary can be detected by consistent long-term monitoring of the source. These periodicities are expected to arise from orbital passages through a gaseous disc, which triggers temporary heightened accretion or shocks in the ambient gas (Bon et al. 2012). Periodic emission may occur at many wavelengths: some from disc interactions in the x-ray or UV and optical, others

from intensified core emission in radio or x-ray. While this technique is observationally intensive, it will play a more important role in the future as a number of high-cadence synoptic surveys come online like the Zwicky Transient Factory (Smith et al. 2014) and LSST (LSST Science Collaboration et al. 2009).

Admittedly, most of the EM signals detected by these surveys will come from sources that do not have resolvable GW signatures, as has been seen in current survey results (Graham et al. 2015). However, comparing predictions for and detections of these signals will provide invaluable insights about the population of binaries that make up the GW stochastic background (Sesana et al. 2017). PTAs may be the only tool that can definitely observe the final stages of binary SMBH evolution (Sesana 2013a), and as such, it is critical that we use all of the observational information available. Given that decoupling the various environmental effects potentially present at the lowest frequencies in the PTA band is very difficult (as seen in Section 4.3), successful interpretation of PTA measurements may require using EM detections and/or non-detections of these sources.

Bibliography

- Abbott, B. P., Abbott, R., Abbott, T. D., et al. 2016, *Physical Review Letters*, 116, 061102
- Allen, B. 1997, in *Relativistic Gravitation and Gravitational Radiation*, ed. J.-A. Marck & J.-P. Lasota, 373
- Arzoumanian, Z., Brazier, A., Burke-Spolaor, S., et al. 2015, *ArXiv e-prints*, arXiv:1508.03024
- Baldry, I. K., Balogh, M. L., Bower, R. G., et al. 2006, *MNRAS*, 373, 469
- Begelman, M. C., Blandford, R. D., & Rees, M. J. 1980, *Nature*, 287, 307
- Beifiori, A., Courteau, S., Corsini, E. M., & Zhu, Y. 2012, *MNRAS*, 419, 2497
- Bernardi, M., Shankar, F., Hyde, J. B., et al. 2010, *MNRAS*, 404, 2087
- Bezanson, R. 2016, private communication
- Bezanson, R., van Dokkum, P., & Franx, M. 2012, *ApJ*, 760, 62
- Bezanson, R., van Dokkum, P. G., Franx, M., et al. 2011, *ApJ*, 737, L31
- Bon, E., Jovanović, P., Marziani, P., et al. 2012, *ApJ*, 759, 118
- Burke-Spolaor, S. 2011, *MNRAS*, 410, 2113
- . 2013, *Classical and Quantum Gravity*, 30, 224013
- Cappellari, M. 2013, *ApJ*, 778, L2
- Chiaberge, M., Gilli, R., Lotz, J. M., & Norman, C. 2015, *ApJ*, 806, 147

- Comerford, J. M., & Greene, J. E. 2014, *ApJ*, 789, 112
- Comerford, J. M., Schluns, K., Greene, J. E., & Cool, R. J. 2013, *ApJ*, 777, 64
- Conselice, C. J. 2014, *ARA&A*, 52, 291
- Creighton, J. D. E., & Anderson, W. G. 2011, *Gravitational-Wave Physics and Astronomy*, 1st edn. (Wiley-VCH Verlag GmbH & Co.)
- Croft, S., & Kaplan, D. 2016, private communication
- Cuadra, J., Armitage, P. J., Alexander, R. D., & Begelman, M. C. 2009, *MNRAS*, 393, 1423
- Ellis, J. 2016, private communication
- Ellison, S. L., Patton, D. R., Mendel, J. T., & Scudder, J. M. 2011, *MNRAS*, 418, 2043
- Enoki, M., & Nagashima, M. 2007, *Progress of Theoretical Physics*, 117, 241
- Graham, A. W. 2016, *Galactic Bulges*, 418, 263
- Graham, M. J., Djorgovski, S. G., Stern, D., et al. 2015, *MNRAS*, 453, 1562
- Gültekin, K., Richstone, D. O., Gebhardt, K., et al. 2009, *ApJ*, 698, 198
- Hartle, J. B. 2003, *Gravity: An Introduction to Einstein's General Relativity*, 1st edn. (Addison-Wesley)
- Hessels, J. W. T., Ransom, S. M., Stairs, I. H., et al. 2006, *Science*, 311, 1901
- Hopkins, P. F., Somerville, R. S., Hernquist, L., et al. 2006, *ApJ*, 652, 864
- Huerta, E. A., McWilliams, S. T., Gair, J. R., & Taylor, S. R. 2015, *Phys. Rev. D*, 92, 063010
- Ilbert, O., McCracken, H. J., Le Fèvre, O., et al. 2013, *A&A*, 556, A55
- Jaffe, A. H., & Backer, D. C. 2003, *ApJ*, 583, 616
- Jenet, F. A., Hobbs, G. B., van Straten, W., et al. 2006, *ApJ*, 653, 1571

- Kaplan, D. L., O'Shaughnessy, R., Sesana, A., & Volonteri, M. 2011, *ApJ*, 734, L37
- Keenan, R. C., Foucaud, S., De Propriis, R., et al. 2014, *ApJ*, 795, 157
- Khan, F. M., Holley-Bockelmann, K., Berczik, P., & Just, A. 2013, *ApJ*, 773, 100
- Khan, F. M., Just, A., & Merritt, D. 2011, *ApJ*, 732, 89
- Kitzbichler, M. G., & White, S. D. M. 2008, *MNRAS*, 391, 1489
- Kocsis, B., & Sesana, A. 2011, *MNRAS*, 411, 1467
- Kormendy, J., Fisher, D. B., Cornell, M. E., & Bender, R. 2009, *ApJS*, 182, 216
- Kormendy, J., & Ho, L. C. 2013, *ARA&A*, 51, 511
- Lentati, L., Taylor, S. R., Mingarelli, C. M. F., et al. 2015, *ArXiv e-prints*, arXiv:1504.03692
- Lotz, J. M., Jonsson, P., Cox, T. J., et al. 2011, *ApJ*, 742, 103
- LSST Science Collaboration, Abell, P. A., Allison, J., et al. 2009, *ArXiv e-prints*, arXiv:0912.0201
- Maggiore, M. 2008, *Gravitational Waves: Volume 1: Theory and Experiments*, 1st edn. (Oxford University Press)
- Mauch, T., & Sadler, E. M. 2007, *MNRAS*, 375, 931
- Mayer, L., Kazantzidis, S., Madau, P., et al. 2007, *Science*, 316, 1874
- McConnell, N. J., & Ma, C.-P. 2013, *ApJ*, 764, 184
- Merritt, D. 2013, *Dynamics and Evolution of Galactic Nuclei*
- Middleton, H., Del Pozzo, W., Farr, W. M., Sesana, A., & Vecchio, A. 2016, *MNRAS*, 455, L72
- Moustakas, J., Coil, A. L., Aird, J., et al. 2013, *ApJ*, 767, 50
- Muzzin, A., Marchesini, D., Stefanon, M., et al. 2013, *ApJ*, 777, 18

- Peters, P. C., & Mathews, J. 1963, *Phys. Rev.*, 131, 435
- Phinney, E. S. 2001, *ArXiv Astrophysics e-prints*, astro-ph/0108028
- Preto, M., Berentzen, I., Berczik, P., & Spurzem, R. 2011, *ApJ*, 732, L26
- Quinlan, G. D. 1996, *New A*, 1, 35
- Ravi, V., Wyithe, J. S. B., Shannon, R. M., & Hobbs, G. 2015, *MNRAS*, 447, 2772
- Ravi, V., Wyithe, J. S. B., Shannon, R. M., Hobbs, G., & Manchester, R. N. 2014, *MNRAS*, 442, 56
- Robotham, A. S. G., Driver, S. P., Davies, L. J. M., et al. 2014, *MNRAS*, 444, 3986
- Rodriguez, C., Taylor, G. B., Zavala, R. T., et al. 2006, *ApJ*, 646, 49
- Roebber, E., Holder, G., Holz, D. E., & Warren, M. 2016, *ApJ*, 819, 163
- Roedig, C., Krolik, J. H., & Miller, M. C. 2014, *ApJ*, 785, 115
- Ryden, B. S. 2016, *Introduction to Cosmology*, 2nd edn. (Cambridge University Press), revised
- Sampson, L., Cornish, N. J., & McWilliams, S. T. 2015, *Phys. Rev. D*, 91, 084055
- Sani, E., Marconi, A., Hunt, L. K., & Risaliti, G. 2011, *MNRAS*, 413, 1479
- Scott, N., Graham, A. W., & Schombert, J. 2013, *ApJ*, 768, 76
- Sesana, A. 2013a, *Classical and Quantum Gravity*, 30, 224014
- . 2013b, *MNRAS*, 433, L1
- Sesana, A., Haardt, F., & Madau, P. 2006, *ApJ*, 651, 392
- Sesana, A., Haiman, Z., Kocsis, B., & Kelley, L. Z. 2017, *ArXiv e-prints*, arXiv:1703.10611
- Sesana, A., & Khan, F. M. 2015, *MNRAS*, 454, L66
- Sesana, A., & Vecchio, A. 2010, *Classical and Quantum Gravity*, 27, 084016

- Sesana, A., Vecchio, A., & Colacino, C. N. 2008, MNRAS, 390, 192
- Shankar, F., Bernardi, M., Sheth, R. K., et al. 2016, MNRAS, arXiv:1603.01276
- Shannon, R. M., Ravi, V., Lentati, L. T., et al. 2015, Science, 349, 1522
- Shen, S., Mo, H. J., White, S. D. M., et al. 2003, MNRAS, 343, 978
- Sheth, R. K., Bernardi, M., Schechter, P. L., et al. 2003, ApJ, 594, 225
- Smailagić, M., & Bon, E. 2015, Journal of Astrophysics and Astronomy, 36, 513
- Smith, R. M., Dekany, R. G., Bebek, C., et al. 2014, in Proc. SPIE, Vol. 9147, Ground-based and Airborne Instrumentation for Astronomy V, 914779
- Tanaka, T., Haiman, Z., & Menou, K. 2010, AJ, 140, 642
- Taylor, E. N., Franx, M., Brinchmann, J., van der Wel, A., & van Dokkum, P. G. 2010, ApJ, 722, 1
- Taylor, S. R., Simon, J., & Sampson, L. 2017, Physical Review Letters, 118, 181102
- Thomas, J., Ma, C.-P., McConnell, N. J., et al. 2016, Nature, 532, 340
- Thorne, K. S. 1987, Gravitational radiation., ed. S. W. Hawking & W. Israel, 330–458
- Tomczak, A. R., Quadri, R. F., Tran, K.-V. H., et al. 2014, ApJ, 783, 85
- van den Bosch, R. C. E. 2016, ApJ, 831, 134
- Vasiliev, E., Antonini, F., & Merritt, D. 2015, ApJ, 810, 49
- Wake, D. A., van Dokkum, P. G., & Franx, M. 2012, ApJ, 751, L44
- Xu, C. K., Zhao, Y., Scoville, N., et al. 2012, ApJ, 747, 85
- Yunes, N., Arun, K. G., Berti, E., & Will, C. M. 2009, Physical Review D, 80, 084001
- Zahid, H. J., Geller, M. J., Fabricant, D. G., & Hwang, H. S. 2016, ApJ, 832, 203

CURRICULUM VITAE

Joseph Simon

Place of birth: Santa Monica, CA

EDUCATION

- 8/2012–8/2017* **Doctor of Philosophy in Physics**
University of Wisconsin – Milwaukee, Milwaukee WI
Advisor: Dr. Xavier Siemens
Honors: Research Excellence Award, UWM Chancellor’s Graduate Student Award
GPA: 3.95/4.00
- 8/2003–5/2007* **Bachelor of Arts in Special Studies (Physics Minor)**
Franklin & Marshall College, Lancaster, PA
Honors: *Cum Laude*, Marshall Scholar, Opdyke Award in Drama, Nolt Award for Musical Excellence, Honor’s & Dean’s List
GPA: 3.55/4.00

RESEARCH EXPERIENCE

- 6/2014–present* **Member of North American Nanohertz Observatory for Gravitational Waves (NANOGrav)**
Associate Member (2014–2015), Full Member (2015–present)
Member of Astrophysics, Detection & Outreach Working Groups
- 8/2013–present* **Graduate Research Assistant**
University of Wisconsin - Milwaukee, Milwaukee WI
Advisor: Dr. Xavier Siemens
NANOGrav Source Modeling
Developed state of the art models for various gravitational wave signals in NANOGrav data, and implement models into data analysis pipelines
Astrophysical Interpretation of NANOGrav Data
Led parts of the astrophysical interpretation for NANOGrav data
NANOGrav Data Analysis
Collaborated on analysis pipeline development and implementation for various types of sources in pulsar timing array data

TEACHING EXPERIENCE

- 8/2012–12/2015* **Teaching Assistant**
University of Wisconsin – Milwaukee, Milwaukee, WI
Lecturer for college algebra
Was the sole lecturer for two sections of Introductory College Algebra
Laboratory instructor for introductory physics courses
Led laboratory instruction for non-calculus based introductory undergraduate physics courses
Discussion section leader for introductory physics courses
Led discussion sections for both calculus and non-calculus based introductory undergraduate courses

FELLOWSHIPS & AWARDS

- 2017* American Physical Society Division of Astrophysics Travel Grant
2016–2017 Distinguished Dissertation Fellowship Recipient (UWM)
2016–2017 Lichtman Research Fellowship Award (UWM)
2015–2017 NASA Wisconsin Space Grant Consortium Fellowship Recipient
2015–2017 David Lichtman Memorial Fellowship Recipient (UWM)

INVITED TALKS

- 3/2016* **CalTech TAPIR Seminar**
California Institute of Technology, Pasadena, CA
Presented on dissertation research.

CONFERENCES AND PRESENTATIONS

APS April Meeting, Washington, DC, Jan. 2017. Oral presentation on Ph.D. research project and publication “Multi-Messenger Sources for Pulsar Timing Arrays”.

229th AAS General Meeting, Grapevine, TX, Jan. 2017. Oral presentation on Ph.D. research project and publication “Multi-Messenger Sources for Pulsar Timing Arrays”.

NANOGrav Fall Meeting, Urbana, IL, Oct. 2016. Oral presentation on Ph.D. research project and publication “Velocity Dispersion Function as Proxies for Black-Hole Mass Function”.

NRAO Lunch Seminar, Socorro, NM, July 2016. Oral presentation on Ph.D. research project, publications “Velocity Dispersion Function as Proxies for Black-Hole Mass Function” and “Multi-Messenger Sources for Pulsar Timing Arrays”.

21st International Conference on General Relativity and Gravitation, New York, NY, July 2016. Oral presentation on Ph.D. research project, publications “Constraints on SMBH/Host Co-evolution” and “Velocity Dispersion Function as Proxies for Black-Hole Mass Function”.

GW Physics & Astronomy Workshop, Hyannia, MA, June 2016. Oral presentation on Ph.D. research project and publication “Constraints on SMBH/Host Co-evolution”.

NANOGrav Spring Meeting, Pasadena, CA, March 2016. Oral presentation on Ph.D. research project and publication “Constraints on SMBH/Host Co-evolution”.

227th AAS General Meeting, Kissimmee, FL, Jan. 2016. Attended the AAS Astronomy Ambassadors Workshop. Oral presentation on Ph.D. research project and publication “Multi-Messenger Sources for Pulsar Timing Arrays”.

NANOGrav Fall Meeting, Montreal, Quebec, Canada, Oct. 2015.

Supermassive Black Hole Workshop, IPTA Meeting, Leura, NSW Australia, July 2015. Oral presentation on Ph.D. research project and publication “Constraints on SMBH/Host Co-evolution”.

UWM CGCA Seminar, Milwaukee, WI, Feb. 2015. Oral presentation on Ph.D. research project.

NANOGrav Student Workshop and Spring Meeting, Arecibo, PR, Feb. 2015.

225th AAS General Meeting, Seattle, WA, Jan. 2015. Poster presentation on Ph.D. research project.

NANOGrav Fall Meeting, Milwaukee, WI, Oct. 2014. Oral presentation on Ph.D. research project.

IPTA Student Workshop and Science Meeting, Banff, Alberta Canada, June 2014.

NANOGrav Spring Meeting, Arecibo, PR, Feb. 2014.

223rd AAS General Meeting, Washington, DC, Jan. 2014. Poster presentation on Ph.D. research project.

PUBLICATIONS

Primary Publications

Joseph Simon and Sarah Burke-Spolaor, *in prep.* “Multi-Messenger Sources for Pulsar Timing Arrays”

Joseph Simon, *in prep.* “Velocity Dispersion Function As Proxies For Black-Hole Mass Function: Implications for Pulsar Timing Arrays”

Stephen R. Taylor, **Joseph Simon**, and Laura Sampson, 2017 “Constraints On The Dynamical Environments Of Supermassive Black-hole Binaries Using Pulsar-timing Arrays,” *Phys. Rev. Lett.* 118 181102

Joseph Simon and Sarah Burke-Spolaor, 2016 “Constraints on SMBH/Host Co-evolution and Binary Stalling Using Pulsar Timing Arrays,” *Ap. J.* 826 11

Joseph Simon, Abigail Polin, Andrea Lommen, et al., 2014 “Gravitational Wave Hotspots: Ranking Potential Locations Of Single-Source Gravitational Wave Emission,” *Ap. J.* 784 60

Collaboration Publications

The NANOGrav Collaboration: Zaven Arzoumanian, ... , **Joseph Simon**, et al., 2016 “The NANOGrav Nine-year Data Set: Limits on the Isotropic Stochastic Gravitational Wave Background.” *Ap. J.* 821 13

The IPTA Collaboration: J. P. W. Verbiest, ... , **Joseph Simon**, et al., 2016 “The International Pulsar Timing Array: First data release.” *Mon. Not. Roy. Ast. Soc.* 458